ARTICLE

Altered projection-specific synaptic remodeling and its modification by oxytocin in an idiopathic autism marmoset model

Jun Noguchi[1*], Satoshi Watanabe[1], Tomofumi Oga[1], Risa Isoda[1], Keiko Nakagaki[1], Kazuhisa Sakai[1], Kayo Sumida[2], Kohei Hoshino[2], Koichi Saito[2], Izuru Miyawaki[3], Eriko Sugano[4], Hiroshi Tomita[4], Hiroaki Mizukami[5], Akiya Watakabe[6], Tetsuo Yamamori[6] & Noritaka Ichinohe[1*]

[1] Department of Ultrastructural Research, National Institute of Neuroscience, National Center of Neurology and Psychiatry, Tokyo, Japan. [2] Environmental Health Science Laboratory, Sumitomo Chemical Co., Ltd., Konohana-ku, Osaka, Japan. [3] Preclinical Research Laboratories, Sumitomo Pharma Co., Ltd., Konohana-ku, Osaka, Japan.[4] Laboratory of Visual Neuroscience, Graduate Course in Biological Sciences, Iwate University, Iwate, Japan. [5] Division of Genetic Therapeutics, Jichi Medical University, Tochigi, Japan. [6] Laboratory for Molecular Analysis of Higher Brain Function, Center for Brain Science, RIKEN, Saitama, Japan.

*Correspondence should be addressed to J.N. (jnoguchi@ncnp.go.jp) or N.I. (nichino@ncnp.go.jp).

ABSTRACT

Alterations in the experience-dependent and autonomous elaboration of neural circuits are assumed to underlie autism spectrum disorder (ASD), though it is unclear what synaptic traits are responsible. Here, we used a valproic acid-induced ASD marmoset model, which shares common molecular features with idiopathic ASD, to investigate the structural dynamics of tuft dendrites of upper-layer pyramidal neurons and adjacent axons in the dorsomedial prefrontal cortex using two-photon microscopy. In model marmosets, dendritic spine turnover was upregulated, and spines were actively generated in clusters and subsequently survived more often than in control marmosets. Presynaptic boutons in local axons but not in commissural long-range axons showed hyperdynamic turnover in model marmosets, suggesting alterations in projection-specific plasticity. Intriguingly, nasal administration of oxytocin reduced the clustered spine emergence. Enhanced clustered spine generation, possibly unique to certain presynaptic partners, may be associated with ASD and may be a potential therapeutic target.

Introduction

Autism spectrum disorder (ASD) is a developmental disorder characterized by impairments in social communication, social interaction, and stereotyped behaviors [1, 2]. Individuals with ASD often have learning disabilities and have difficulty learning to recognize verbal or non-verbal social information [3]. Proper refinement of neural networks during learning is achieved by coordinated synaptic remodeling, which may be altered in ASD. Dendritic spines, which are postsynaptic protrusions that receive most excitatory inputs [4-6], have been observed longitudinally using two-photon microscopy in mouse models of ASD. This has made it possible to explore the spatiotemporal characteristics of synaptic remodeling in ASD. Morphological analysis of dendrites with in vivo two-photon microscopy has shown that accelerated spine generation and elimination in the motor and primary sensory cortices is a consistent phenotype in numerous ASD

45 mouse models (BTBR, 15q11-13 duplication, Neuroligin mutant, *FMR1* knockout, *MeCP2*
46 duplication, etc.) [7-10].
47
48 Clustered generation of postsynaptic dendritic spines, in which new spines form in close
49 proximity to one another, plays a critical role in learning and memory [11-17]. Training increases
50 clustered spine generation, which has been found to be correlated with learning performance in
51 corresponding brain regions [10, 18]. Neuronal modeling studies have suggested that enhanced
52 clustered spine generation increases memory discrimination and the storage capacity of neuronal
53 networks [17, 18]. Excessively clustered spines may contribute to the development of ASD symptoms,
54 but little is known about their involvement in this condition. On the other hand, it has been
55 reported that diversity of excitatory synapses includes several synapse types or subtypes defined
56 by molecular and other characteristics, and that certain circuits or connectome networks prefer
57 particular types of synapses [19]. Changes in gene expression in ASD may alter the plasticity of
58 specific cortical projections, which may in turn perturb the formation of neural circuits adapted
59 to learning. However, projection-specific variations of synapse remodeling in ASD have not been
60 explored.
61
62 The common marmoset (*Callithrix jacchus*), a small New World monkey, has attracted
63 significant attention due to its rich repertoire of social behaviors, a well-developed prefrontal
64 cortex (PFC) that supports high-level social ability, and gene expression networks that are similar
65 to those in humans [20]. In fact, marmosets are more similar to humans than rodents in terms of their
66 synaptic proteome [21]. We previously developed a valproic acid (VPA)-induced ASD model in the
67 common marmoset [22]. VPA is an antiepileptic drug and also functions as a histone deacetylase
68 inhibitor that may epigenetically increase the risk of ASD in humans by suppressing histone
69 deacetylases in the fetal brain. Despite the fact that VPA administration was the sole
70 environmental factor contributing to the development of ASD in this model, and there were no

genetic variations, it was sufficient to induce gene expression changes in juvenile marmosets that were more typical of human idiopathic ASD than those in monogenetic ASD rodent models [22]. The characteristics of VPA-exposed marmosets suggest that these ASD models may be useful for bridging rodent ASD studies and human ASD.

In this study, we investigated the temporal remodeling of neural circuits using in vivo two-photon longitudinal imaging in VPA-exposed adult marmosets. We analyzed synaptic dynamics at 3-day intervals in the apical tuft dendrites of pyramidal neurons in the primate-specific dorsomedial PFC (dmPFC). The dmPFC is involved in social cognition and habit formation, and was found to exhibit less activity in nonverbal information-biased judgment in ASD individuals [23]. We also observed the axonal boutons of local and long-distance cortical callosal connections labeled with fluorescent proteins of different colors to investigate whether circuit-specific synaptic remodeling was altered in the ASD model animal. Our study revealed that in VPA-exposed marmosets, turnover of postsynaptic dendritic spines was upregulated, and spines were actively generated in clusters but seemed to be randomly eliminated. Notably, in the marmoset model, the rates of both generated clustered spines and subsequently surviving spines (carryover spines) were much higher than in controls (3.3 and 5.9 fold, respectively). Presynaptic boutons of local axons, but not long-range commissural axons, showed more frequent turnover in model marmosets than in controls. Importantly, the clustering propensity of emergent spines in VPA-exposed marmosets was reduced by intranasal administration of oxytocin, which is currently being tested as a therapy for human ASD. These results suggest that both enhanced generation of clustered spines and altered turnover of local neuronal circuits are associated with ASD. We consider that these processes may be potential therapeutic targets for ASD symptoms.

Results

Two-photon imaging of the dendrites of PFC layer-2/3 pyramidal neurons in living marmosets

97 Changes in spine geometry (density) have been observed in the brains of individuals with ASD
98 [24], and alterations in synaptic electrophysiological characteristics have been reported in animal
99 models of ASD [22, 25]. In the present study, we used a marmoset ASD model to investigate spine
100 dynamics in the dmPFC. We used three adult VPA-exposed marmosets and four adult unexposed
101 (UE) marmosets (See **Methods**). We inoculated the marmoset dmPFC with adeno-associated
102 virus (AAV) and expressed fluorescent proteins mainly in layer-2/3 pyramidal neurons [26]. These
103 proteins showed sufficient fluorescence for in vivo two-photon imaging. The fluorescent protein-
104 expressing neurons were locally distributed with an average diameter of 1.81 mm (range: 1.02-
105 2.87) axially and 1.53 mm (range: 0.86-2.21) laterally. Post-experiment immunohistochemistry
106 using antibodies against Iba-1 and GFAP showed no obvious increases in activated microglia or
107 astrocytes, respectively (Figure S1).
108
109 We performed time-lapse observation of the dmPFC using a two-photon microscope [26, 27] (Figures
110 1A and 1B). Every 3 days, we conducted three imaging sessions of identical apical tuft dendrites
111 in UE and VPA-exposed animals (n = 14 and 12 dendrites, respectively; mean dendrite span per
112 branchlet: 31.7 ± 5.9 μm and 31.6 ± 5.8 μm, respectively). We found no significant differences in
113 the dendritic spine density on apical tuft dendrites between the two types of marmosets (Figure
114 1C). We next compared the spine generation and elimination rates between the VPA-exposed and
115 UE groups (Figures 1B and 1D). We found that the rates of both spine generation and elimination
116 were approximately two times higher in VPA-exposed than UE marmosets (Figure 1D). This
117 result was consistent with the results from various ASD mouse models of enhanced spine
118 generation and elimination [7-10].
119
120 **Smaller spines in the ASD model marmoset were more prone to elimination**
121 We next performed an analysis of spine volume, which is a crucial measure of synaptic weight.
122 We calculated the normalized spine volume by dividing each spine's fluorescent intensity with

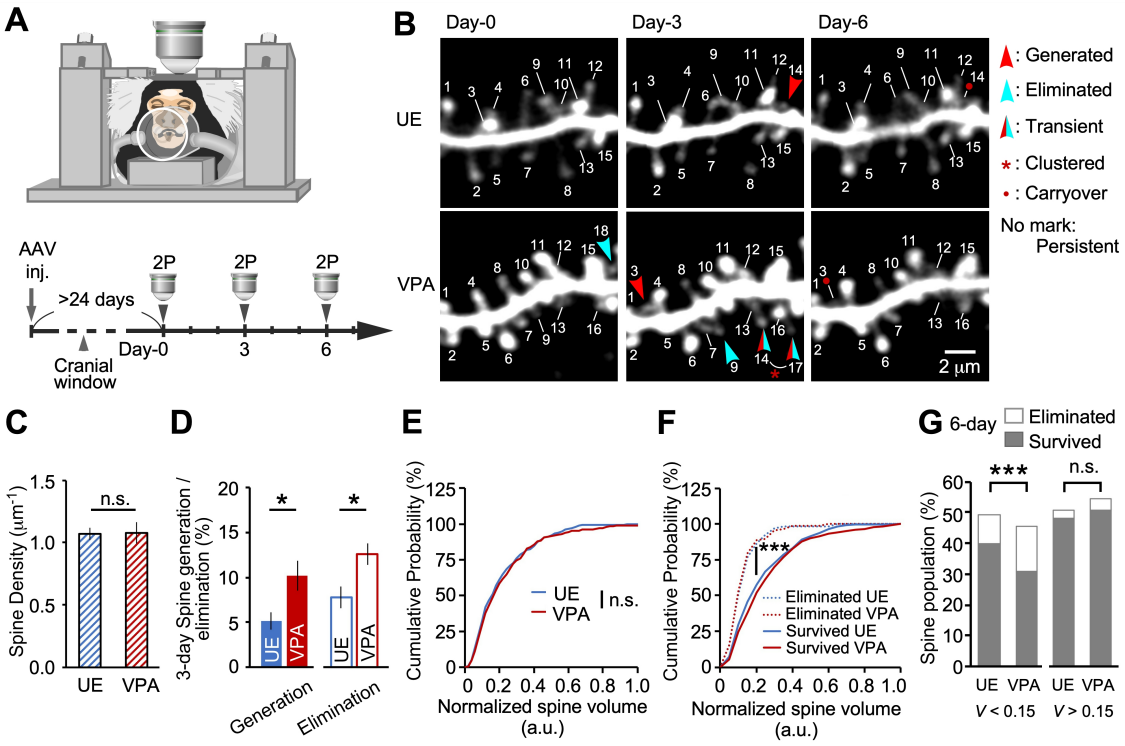

Figure 1. In vivo two-photon imaging of mature marmoset dendrites. (**A**) A marmoset was anesthetized for two-photon (2P) imaging. The lower panel shows the experimental schema. (**B**) Longitudinal 2P imaging from the PFC layer-2/3 pyramidal neuron tuft dendrites. Every 3 days, the same dendrites were imaged in UE (unexposed; control animals) and VPA-exposed (ASD model) marmosets, and the same spines were labeled using the same numbers throughout the period. (**C**) Mean spine densities of dendrites (mean ± s.e.m.; $P = 0.85$, Mann-Whitney U test; $n = 14$ and 12 dendrites in four and three UE and VPA-exposed animals, respectively). (**D**) Three-day spine generation rates (mean ± s.e.m.; $P = 0.047$, Mann-Whitney U test; the same dendrites as in (C)), and 3-day elimination ($P = 0.044$). (**E** and **F**) Cumulative plots of the normalized spine volume distribution (E) ($P = 0.72$; Kolmogorov-Smirnov test; $n =$ 536 and 473 spines in UE and VPA-exposed animals, respectively), and cumulative plots of eliminated UE, eliminated VPA-exposed, surviving UE, and surviving VPA-exposed spines during the 6-day observation (F) ($P <$ 0.001; $n = 65$, 87, 471, and 386 spines, respectively). (**G**) The population of eliminated and surviving spines during the 6-day observation are shown separately for groups with a spine volume of $V < 0.15$ and $V > 0.15$ ($V < 0.15$; $P <$ 0.001; Fisher's exact test; $n = 50$, 69, 214, and 146 spines as in (F)) ($V > 0.15$; $P = 0.59$; $n = 15$, 18, 257, and 240 spines as in (F)). ***$P < 0.001$; *$P < 0.05$; n.s., not significant.

the dendrite shaft intensity, and pooled the results of all dendrites. The results showed no significant difference in the distribution of spine volume between the VPA-exposed and UE groups (Figure 1E). As in previous studies [28, 29], both groups showed a significant difference in volume distribution between spines that were eliminated during the 6-day period and those that survived (Figure 1F). The volume distribution of the VPA-exposed and UE groups did not differ when the eliminated and surviving groups were analyzed separately (Figure 1F); however, for the smaller spines, the proportion of eliminated spines was significantly larger in the VPA-exposed

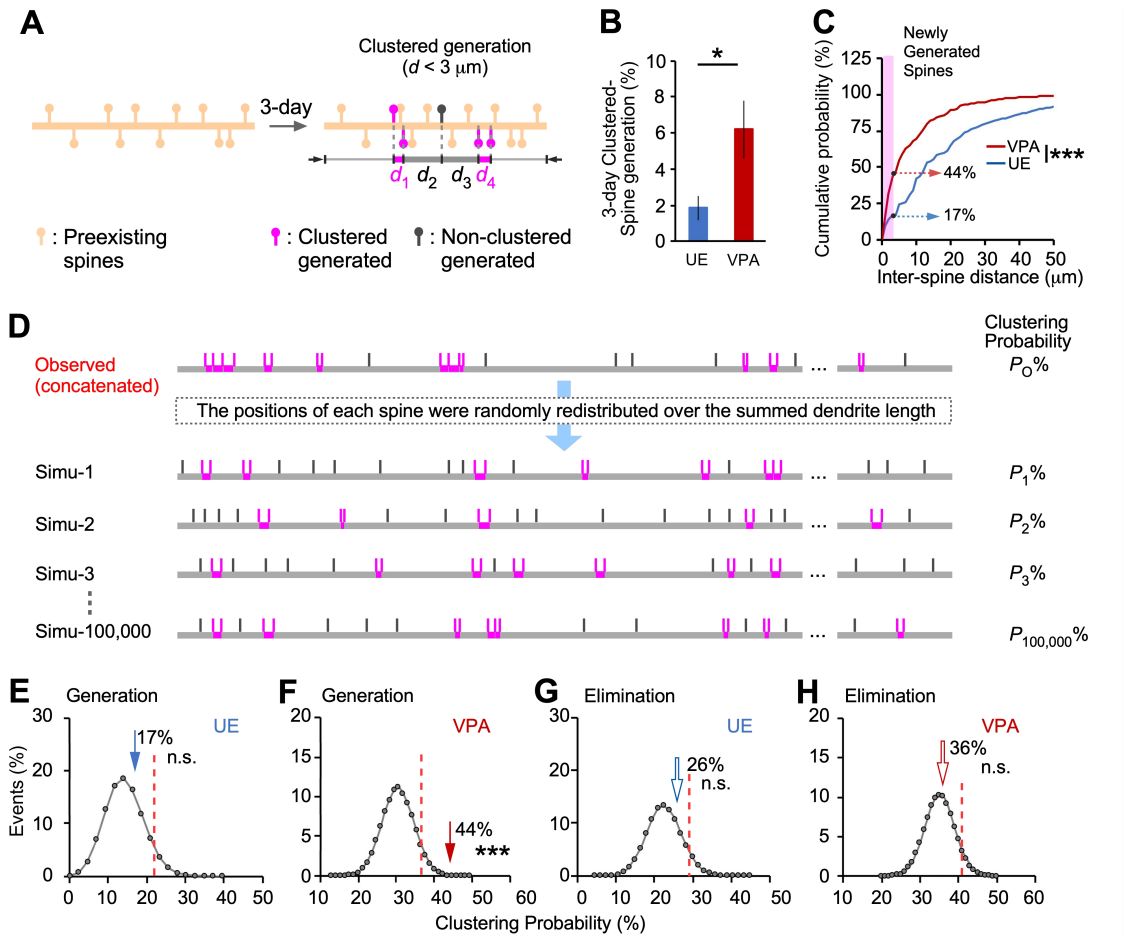

Figure 2. Dendritic spine clustered generation is more predominant than clustered elimination in VPA-exposed marmosets. (**A**) Schematic drawing of clustered spine generation. Pairs of newly generated or eliminated spines were considered to be clustered if they occurred within 3 μm of each other. Spines colored magenta or gray represent clustered and non-clustered spines, respectively. (**B**) Comparison of the percentage of clustered generated spines to the total number of spines between UE and VPA-exposed animals (mean ± s.e.m.; $P = 0.016$, Mann-Whitney U test; $n = 14$ and 12 dendrites in four UE and three VPA-exposed animals, respectively). (**C**) Distribution of inter-spine distances between newly generated spines ($P = 0.0009$; Kolmogorov-Smirnov test; $n = 45$ and 85 spine pairs in UE and VPA-exposed animals, respectively). Magenta-shaded area indicates inter-spine distances shorter than 3 μm, and numbers indicate the probabilities of clustering (within 3 μm). To prevent underestimation of the inter-spine distance, dendrites were concatenated into one long dendrite. (**D**) Validation of clustering bias by Monte Carlo simulation. In the simulation, the new spine positions were randomly determined with a uniform distribution over the summed dendrite length. Clustering probabilities for all inter-spine distances were calculated for each simulation, and the distributions of the clustering probability from 100,000 iterations are shown in (**E**)-(**H**). (E–H) Circles connected with gray lines represent probability plots of clustering events from 100,000 simulations; the actual numbers of spine clusters are represented by arrows ($P = 0.23$ and 0.00042; $n = 44$ and 86 newly generated spines in 14 and 12 dendrites in UE and VPA-exposed animals, respectively) ($P = 0.20$ and 0.36; $n = 68$ and 100 newly eliminated spines in UE and VPA-exposed animals, respectively). Dotted red lines show 95th percentiles. ***$P < 0.001$; *$P < 0.05$; n.s., not significant.

group (Figure 1G). These results suggest that the synaptic weight distributions in the dendrites were similar in the two types of marmosets, whereas the smaller spines were more vulnerable in

132 VPA-exposed animals.

133

134 **Newly generated spines clustered more frequently in VPA-exposed marmosets than in**
135 **controls**

136 The generation of spines in close proximity to each other, or clustered spine generation, is
137 considered to have functional significance, especially in learning and memory [5, 10, 15, 18]. We next
138 examined whether the generated spines in the VPA-exposed and UE marmosets were clustered
139 or not (Figure 2A). We chose a 3 μm window for our analyses, since several biochemical,
140 physiological, and structural studies have suggested that a 3 to 10 μm distance between spines
141 facilitates sharing of resources, spine co-activation, and learning-induced structural plasticity [30-
142 36]. Moreover, the difference between the UE and VPA-exposed animals in spine clustering
143 reached a plateau at a distance of 3 μm between spines, suggesting that events occurring within 3
144 μm are particularly important (Figure S2A). Clustered spine generation occurred 3.3 times more
145 frequently in VPA-exposed animals than in UE animals (Figure 2B), even though the total number
146 of generated spines in VPA-exposed marmosets was only about twice as many as that in the UE
147 marmosets (Figure 1D). The clustered generated spines even accounted for 6.2% of the total
148 spines on the dendrites. Next, we created a cumulative plot of the distance between generated
149 spines. As shown in Figure 2C, there was a significant difference in the distribution of interspine
150 distances between the VPA-exposed and UE groups. Again, the difference between the VPA-
151 exposed and UE animals in terms of the probability of clustered spine generation was large (2.6
152 fold; Figure 2C). These results suggest the existence of a mechanism by which dendritic spines
153 actively appear in clusters in the animals exposed to VPA. Therefore, we conducted a Monte
154 Carlo simulation experiment to determine whether there was more clustering bias in VPA-
155 exposed marmosets than in the hypothetical uniform random spine distribution (Figure 2D). To
156 prevent underestimation of the inter-spine distances between the newly generated and eliminated
157 spines, we conducted a simulation with all measured dendrites concatenated into one long

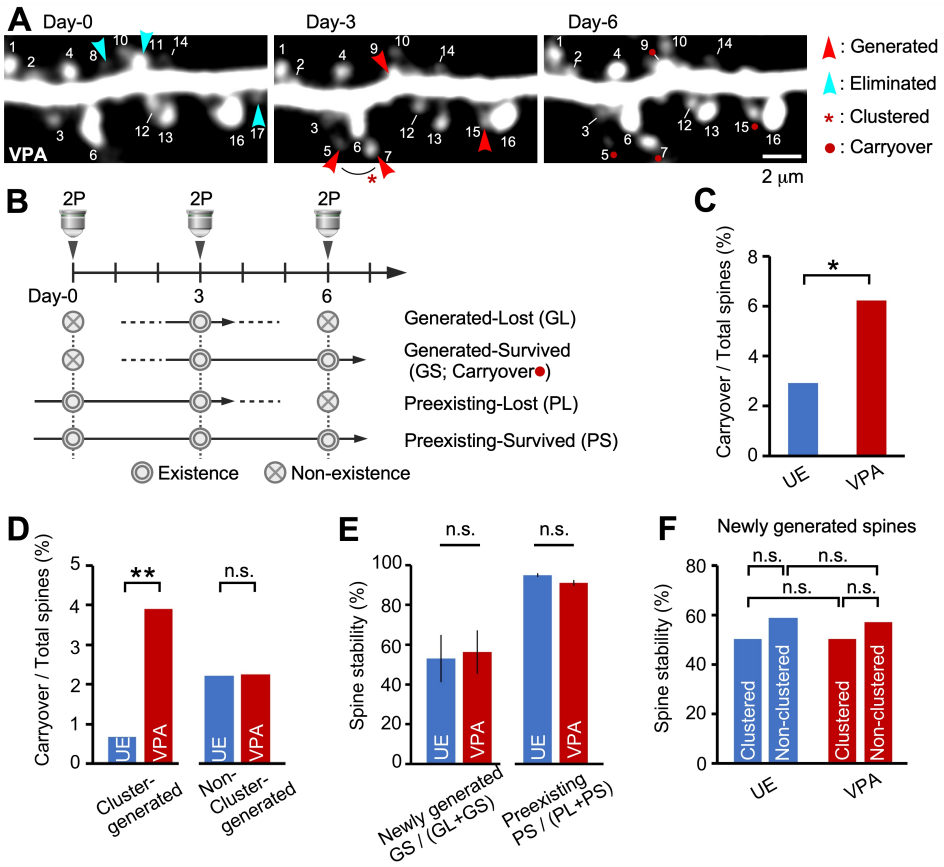

Figure 3. The surviving fraction of newly generated spines (carryover spines) is much larger in VPA-exposed marmosets than in controls, although spine stability is similar. (**A**) Representative dendrite images taken every 3 days are presented as in Fig. 1B. (**B**) A diagram showing four patterns of spine generation and elimination. The red dot in the legend indicates the carryover spines labeled with a red dot in Figs. 1B and 3A. (**C**) The ratio of the surviving fraction of newly formed spines (carryover spines) to the total spines was larger in VPA-exposed animals than in UE animals. ($P = 0.037$, Fisher's exact test; $n = 13$, 448, 22, and 355 for UE carryover spines, UE total spines, VPA-exposed carryover spines, and VPA-exposed total spines, respectively). (**D**) Among clustered generated spines, the ratio of the carryover spine fraction to the total spines was much larger in VPA-exposed animals than in UE animals ($P = 0.0022$, Fisher's exact test; $n = 3$, 448, 14, and 355 for UE carryover, UE total, VPA-exposed carryover, and VPA-exposed total spines, respectively). By contrast, the carryover spine fraction was not significantly different among non-clustered spines ($P > 0.99$, Fisher's exact test; $n = 10$, 448, 8, and 355 for UE carryover, UE total, VPA-exposed carryover, and VPA-exposed total spines, respectively). (**E**) The stability of each newly generated and pre-existing spine was not significantly different between UE and VPA-exposed animals (mean ± s.e.m.; $P = 0.94$ and $P = 0.091$; Mann-Whitney U test; $n = 13$ and 10 dendrites from three UE and three VPA-exposed animals, respectively). (**F**) The stability of each newly formed spine was not significantly different between the clustered and non-clustered spines ($P > 0.99$; Fisher's exact test; $n = 3$, 10, 3, and 7 for clustered GS, non-clustered GS, clustered GL, and non-clustered GL spines, respectively, in UE animals) ($P > 0.99$; Fisher's exact test; $n = 14$, 8, 14, and 6, respectively, in VPA-exposed animals). $^{**}P < 0.01$; $^{*}P < 0.05$; n.s., not significant.

dendrite, where dendrite lengths and spine counts of each dendrite were summed. The difference in clustering probability of the generated spine pairs between the UE and VPA-exposed animals was much larger than that of the eliminated spine pairs. In addition, the clustering probability of

161 the generated spine pairs was greater than the 95th percentile of the simulation distribution in the
162 VPA-exposed group (Figure 2F), but remained below the 95th percentile in the UE group (Figure
163 2E). The clustering probability of the eliminated spine pairs did not exceed the 95th percentile in
164 either the UE group (Figure 2G) or the VPA-exposed group (Figure 2H). Considering that the
165 generated clustered spines may appear on specific dendrites, we conducted another simulation in
166 which the dendrite length and the number of spines generated on each dendrite were left unaltered
167 (that is, each dendrite was treated separately without concatenation), and obtained similar results
168 (Figures S2D-H). We conclude that the clustering of newly generated spines, but not that of
169 eliminated spines, on the dendrites of VPA-exposed marmosets is substantially enhanced rather
170 than randomly distributed.
171
172 **The carryover fraction of newly generated clustered spines was higher in VPA-exposed**
173 **marmosets than in controls**
174 Three consecutive imaging sessions allowed us to monitor the fate of pre-existing and newly
175 generated spines over 3 days [9]. The carryover fraction was defined as the fraction of newly
176 generated spines that survived to the last session (Figures 3A and 3B, GS). The carryover fraction
177 was two times higher in VPA-exposed marmosets than in UE marmosets (Figure 3C). This
178 suggests that experience-induced changes in spines may be more likely to persist in VPA-exposed
179 marmosets. We further divided the newly generated spines into clustered and non-clustered spines
180 and computed their carryover fractions. The carryover fraction of clustered spines in VPA-
181 exposed marmosets was 5.9 times higher than that in UE marmosets (Figure 3D). On the other
182 hand, there was no difference in the carryover fraction of non-clustered spines with or without
183 VPA treatment (Figure 3D). Thus, clustered spines accounted for a greater proportion of spine
184 carryover in the model marmosets than in the UE marmosets.
185

186 Having analyzed the collective nature of spines, we next analyzed the temporal stability of
187 individual spines. Spine stability was defined as the percent ratio of newly generated or pre-
188 existing spines that survived to the last session. Both in the VPA-exposed and UE groups, the
189 spine stability of newly generated spines (~50%) was considerably lower than that of pre-existing
190 spines (~90%) (Figure 3E). However, the stability of these two types of spines did not differ
191 between the VPA-exposed and UE groups (Figure 3E). Furthermore, spine stability in both the
192 VPA-exposed and UE groups was independent of the presence or absence of clustering (Figure
193 3F). The fact that spine stability was the same regardless of clustering suggests that interactions
194 among newly formed spines have little effect on spine stability for some time after spine
195 generation. In summary, clustered carryover spines comprised a much higher proportion of total
196 spines in the VPA-exposed marmosets than in the UE animals, while the stability of individual
197 spines was equivalent in the two groups.
198
199 Lastly, we compared the clustering of VPA-exposed marmosets with those of a mouse model.
200 Exaggerated clustering of generated spines has been reported in a mouse model of *MeCP2* gene
201 duplication, which results in a rare syndrome with core symptoms of ASD [10]. The mean values of
202 clustered emergent spines in the mouse study were obtained from the graphs in the paper. The
203 results showed that the frequency of clustered emergent spines in the VPA-exposed marmosets
204 was 9.4 per 100 μm, which was 3.9 times higher than that in *MeCP2* duplication mice (2.4 per
205 100 μm) (Figure S2B). Like the clustered spine generation rate, the carryover fraction in VPA-
206 exposed marmosets was much higher than reported in *MeCP2* duplication mice. The frequency
207 of carryover spines that appeared in clusters was 5.3 per 100 μm in the VPA-exposed marmosets,
208 which was 5.7 times higher than in the *MeCP2* duplication mice (0.9 per 100 μm). Thus, the rate
209 of spine clustering in the marmoset model differed markedly in comparison to the *MeCP2*
210 duplication mouse model.
211

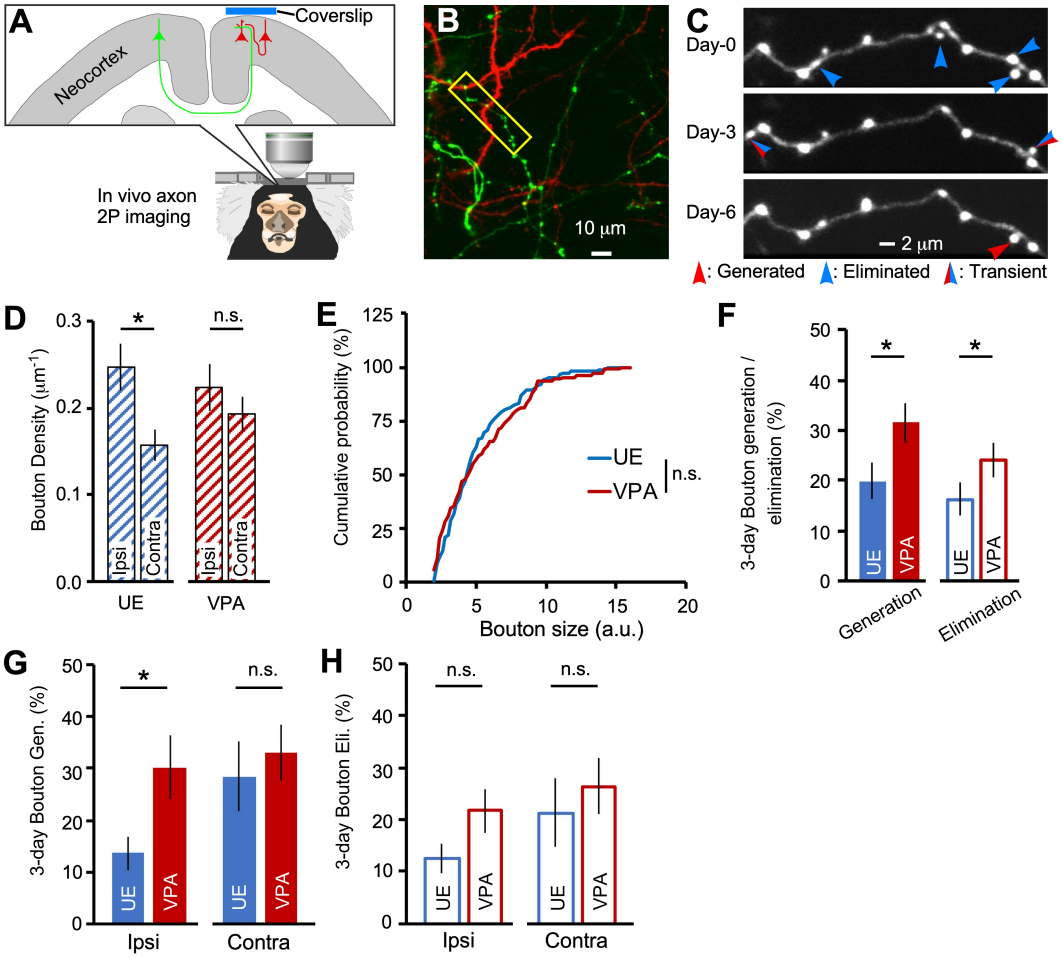

Figure 4. Two-photon in vivo axon imaging in ASD model marmosets. (**A**) AAV vectors expressing different colored fluorescent proteins were inoculated into each hemisphere of the dmPFC. (**B**) Axons from the contralateral hemisphere had green fluorescence, and axons from the ipsilateral hemisphere and dendrites had red fluorescence. (**C**) A representative axon from a VPA-exposed animal (the axon surrounded by the yellow rectangle in (B)) was imaged every 3 days. (**D**) Mean bouton densities are significantly larger in ipsilateral axons than in contralateral axons in UE animals ($P = 0.035$, Mann-Whitney U test; $n = 28$ and 21 ipsilateral and contralateral axons, respectively, from three animals). They are not significantly different between ipsilateral and contralateral axons in VPA-exposed animals ($P = 0.36$; $n = 22$ and 25 ipsilateral and contralateral axons, respectively, from two animals). The mean densities of terminal boutons were much lower than those of en passant boutons in our sample (mean terminal bouton density: 0.023, 0.012, 0.021, and 0.010 boutons/μm for UE ipsilateral, UE contralateral, VPA-exposed ipsilateral, and VPA-exposed contralateral axons, respectively). (**E**) The bouton size distribution between these animals ($P = 0.57$; Kolmogorov-Smirnov test; $n = 149$ and 107 boutons in 49 and 47 axons in three and two UE and VPA-exposed animals, respectively). (**F**) There is a significant difference in three-day bouton generation rates between these animals ($P = 0.012$, Mann-Whitney U test; $n = 49$ and 47 axons in three and two UE and VPA-exposed animals, respectively), and also in 3-day bouton elimination ($P = 0.043$). (G and H) Three-day mean bouton generation rates (**G**) (mean ± s.e.m.; $P = 0.018$ and $P = 0.49$, Mann-Whitney U test; $n = 28$, 22, 21, and 25 for UE ipsilateral, VPA-exposed ipsilateral, UE contralateral, and VPA-exposed contralateral axons, respectively) and elimination rates (**H**) ($P = 0.093$ and $P = 0.28$) for each axon type. *$P < 0.05$; n.s., not significant.

212

213 **Axonal boutons had a higher turnover rate in VPA-exposed marmosets than in controls**

214 Deficits in projection-specific connectivity or cortical interaction have often been discussed in
215 ASD, as exemplified by local overconnectivity and long-range underconnectivity [37-39]. Spine
216 turnover may depend on which neuron the coupled axons originate from [7]. We next analyzed
217 marmoset axons that were transfected with colored fluorescent proteins that differed according to
218 the dmPFC hemisphere from which they projected (Figure 4A). We expressed the red fluorescent
219 protein tdTomato in neurons ipsilateral to the observation window in the PFC, and the green
220 fluorescent protein mClover in neurons on the contralateral side (same axial position and same
221 distance from the midline; Figure 4A). Therefore, we were able to observe red dendrites and red
222 axons from local neurons, as well as green axons from contralateral neurons (Figure 4B). In the
223 magnified images, varicosities called presynaptic boutons were seen on the axons; new generation
224 and elimination of these varicosities were seen on each of the three observation days (Figure 4C).
225 Previous studies have shown that these boutons constitute presynapses [40], although some
226 presynaptic terminals lack distinct varicosities (i.e., boutons) on the axons. In the present sample,
227 most boutons were *en passant* boutons, and relatively few terminal boutons which had a neck
228 between a varicosity and a parental axon shaft (Figure 4C). In this study, we considered the
229 boutons to represent the existence of presynapses. We first measured the axonal bouton density
230 and found a significant difference between the mean values of the ipsilateral and contralateral UE
231 marmoset axons. By contrast, the difference between the ipsilateral and contralateral axons in
232 VPA-exposed marmosets was not significant (Figure 4D). Next, we calculated the bouton size,
233 which represents the synaptic weight [40], under the assumption that it was proportional to the
234 maximum fluorescence intensity. We found that the distribution of bouton size was almost
235 identical between the VPA-exposed and UE groups (Figure 4E). The size distribution was
236 consistent in both spines and boutons, indicating that the balance of excitatory neuronal inputs is
237 maintained in this autism model. We then calculated the 3-day bouton generation and elimination
238 rates. Consistent with the rates of spine generation and elimination, those of bouton generation

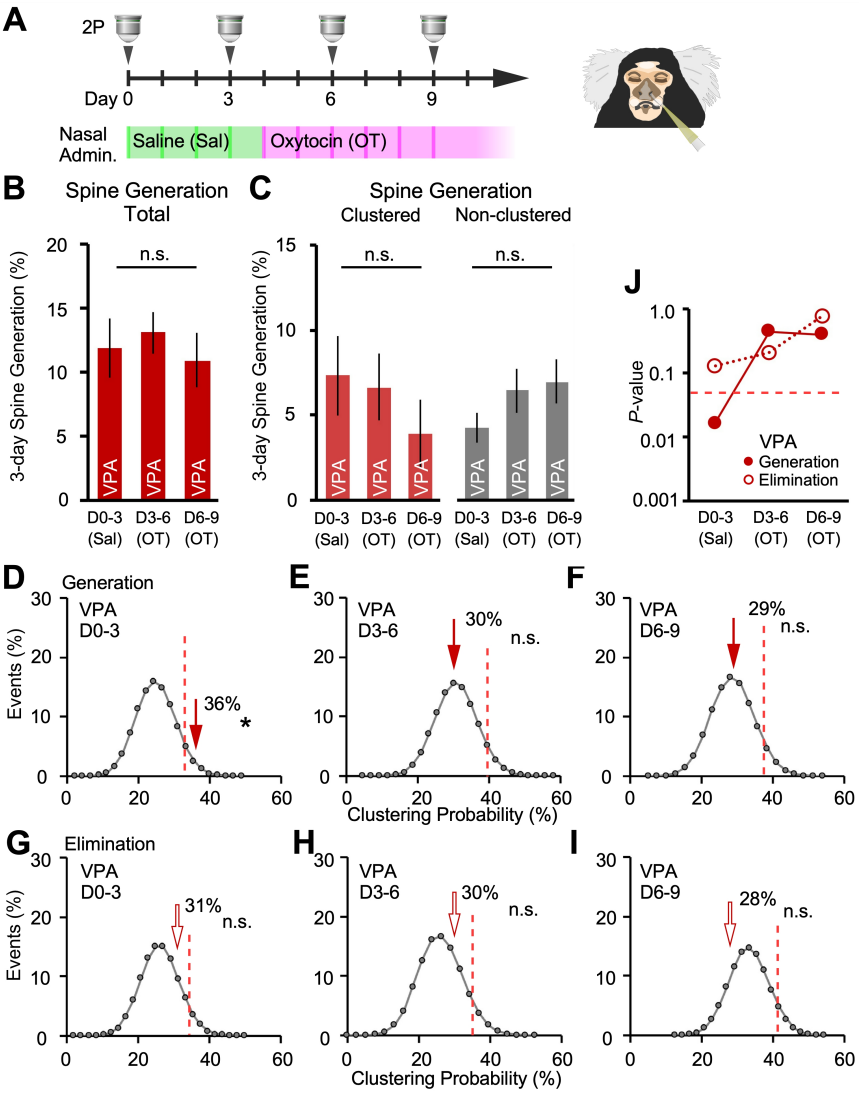

Figure 5. Oxytocin modifies the proximity of spine generation in model marmosets.
(**A**) Schematics of oxytocin nasal administration and two-photon (2P) imaging (Left panel) and transnasal administration using a micropipette (Right panel). Saline was given to marmosets in the green-shaded period, while oxytocin was given in the magenta-shaded period. (**B**) Three-day spine generation rates were not modified after oxytocin administration (mean ± s.e.m.; $P = 0.34$, Friedman test; $n = 12$ dendrites in three VPA-exposed animals). (**C**) Three-day clustered or non-clustered spine generation rates were markedly (but not significantly) modified after oxytocin administration (mean ± s.e.m.; $P = 0.22$ and $P = 0.56$ for clustered and non-clustered spine generation, respectively, Friedman test; $n = 12$ dendrites in three VPA-exposed animals). (**D–I**) Effects of oxytocin on clustering bias of newly generated (D–F) and eliminated (G–I) spines. The graphs are shown as in Figs. 2E–H. ($n = 45$, 43, and 39 newly generated spine pairs and $n = 48$, 38, and 48 newly eliminated spine pairs during the D0–3, D3–6, and D6–9 periods, respectively, in three VPA-exposed animals). Dotted red lines show 95th percentiles. (**J**) The P-values expressed in logarithm from (D)–(I) are indicated. *$P < 0.05$; n.s., not significant.

239 and elimination were higher in VPA-exposed animals (Figure 4F). Detailed analysis of each type
240 of axon showed a significant difference in ipsilateral bouton gain between the two groups,
241 whereas there was no significant difference in contralateral bouton gain (Figure 4G). This

242 suggested that the difference in the generation and elimination of synapses between the VPA-
243 exposed and UE groups may have been caused by the alteration of ipsilateral (i.e., local) axons.
244 The 3-day bouton turnover rate was higher than that of spines (spine: 10.2% and 12.6% for VPA-
245 exposed group, 5.2% and 7.8% for UE group, for generation and elimination, respectively). These
246 results suggest that a mechanism that regulates appropriate synaptic remodeling in a projection-
247 specific manner exists in control animals and that it is disrupted (hyperdynamic turnover in the
248 local circuits) in the ASD model.
249
250 **Oxytocin nasal administration modified dendritic spine clustering**
251 Oxytocin, a prosocial neuropeptide, is a potentially effective treatment for ASD symptoms.
252 Oxytocin modifies the social skills of typically developed human individuals, and improves
253 sociality in mouse ASD models [41-43]; therefore, its potential as a therapeutic agent for ASD has
254 long been anticipated. However, the benefits of oxytocin in human clinical trials are currently
255 inconclusive [44-47]. In order to better understand the clinical applications of oxytocin, it is therefore
256 important to investigate its mechanism of action on synaptic phenotypes, which were
257 characterized in this study in VPA-exposed marmosets. Thus, we next examined how the
258 aforementioned properties of cortical spines changed after the administration of oxytocin.
259 Oxytocin receptors have been shown to be expressed in the mouse cerebral cortex presynapse and
260 postsynapse of putative excitatory neurons, but are not yet known in marmosets[48-50]. We have
261 demonstrated the presence of the oxytocin receptor protein through Western blot analysis within
262 the synaptosomal fraction isolated from the gray matter of the adult marmoset prefrontal cortex
263 (Figure S5). Marmosets were administered saline and then oxytocin, both intranasally (Figure
264 5A). The average results from all marmosets failed to show a significant effect of oxytocin on
265 spine generation and elimination rates (Figures 5B and S3A). Alternatively, analysis of the
266 distance between generated spines suggested that oxytocin may affect the clustering efficiency of
267 newly generated spines (Figures S3C and S3D). Thus, we next examined the effect of oxytocin

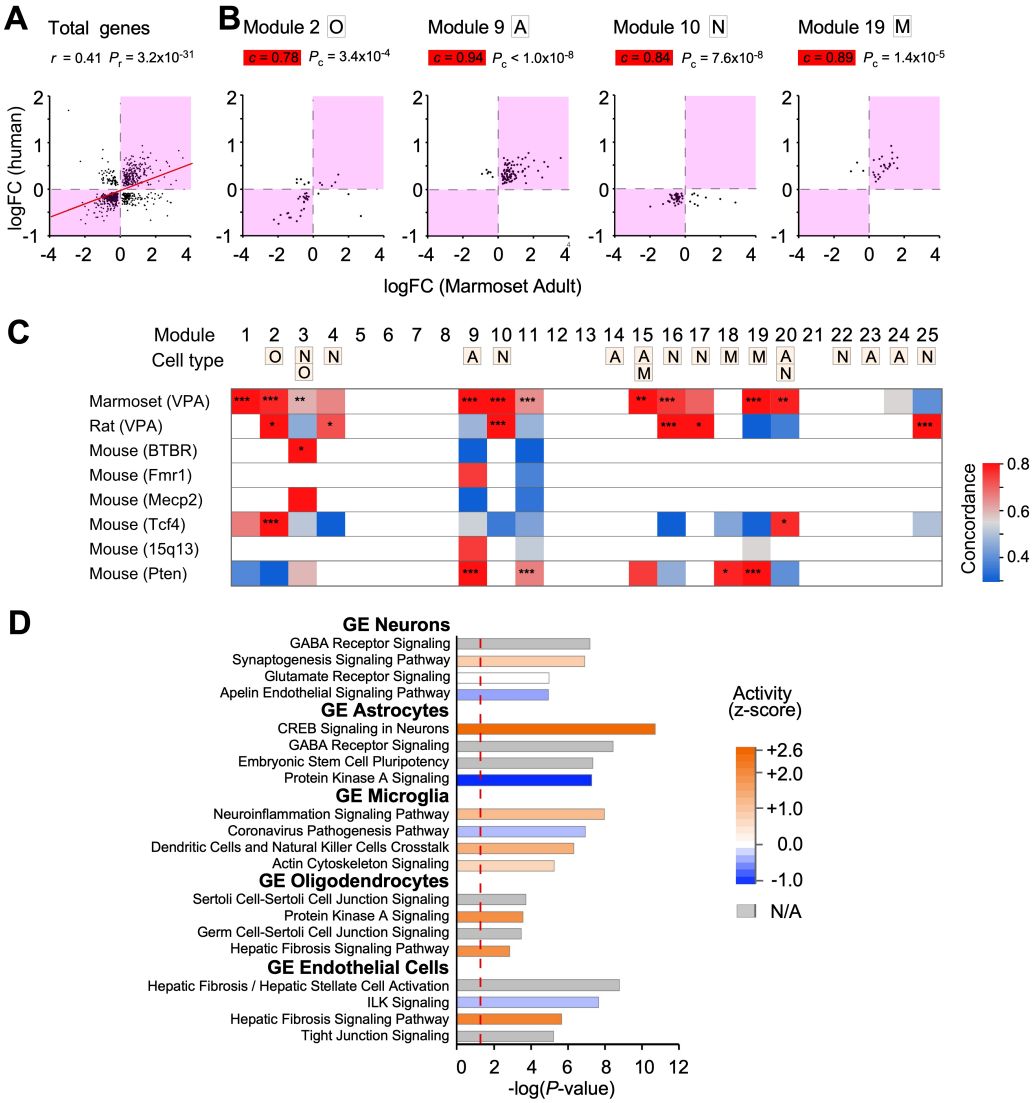

Figure 6. Gene expression modulations in adult marmoset social neocortical areas reflect those in human ASD as determined by microarray analysis. (**A, B**) Relationship of gene expression modulation between adult marmosets and postmortem samples from humans with ASD (A, B). As a measure of gene expression modulation, log fold-change (logFC) values were computed between ASD model animals and control animals, and then compared with human ASD data. Modulated genes with $P_{adj} < 0.1$ are plotted. Pearson's correlation coefficient (r) and the P-values for the correlation coefficient (P_r) are shown in (A). As a measure of concordance in the direction of gene expression modulation, one-sided P-values for concordance (P_c) are shown in (B). The magenta-shaded areas represent the first and third quadrants, indicating that the two elements have changed in the same positive or negative direction. The red line in (A) is the linear regression. (**C**) Concordance of gene expression modulations across human modules. The color indicates concordance between animal model and human ASD modules with at least eight genes in common. Asterisks represent P-values determined using the one-sided binomial test: $*P < 0.05$, $**P < 0.01$, $***P < 0.001$. For the rat VPA-exposed model and BTBR mice, genes with $P_{adj} < 0.05$ were selected; for other models and human ASD, those with $P_{adj} < 0.1$ were selected. (**D**) Enriched pathways for each cell type. The genes most closely associated with neurons, astrocytes, microglia, oligodendrocytes, and endothelial cells were analyzed. The color of the bars represents the direction of regulation of the pathway based on the logFC values. The P-values of enrichment were provided by the IPA software. The red dotted line represents the significance threshold ($P = 0.05$); N/A, not available.

268 administration on spine clustering (Figures 5C-J). After the oxytocin treatment period began, the

269 proportion of clustered generated spines gradually decreased while that of non-clustered
270 generated spines increased, although the difference was not significant (Figure 5C). We therefore
271 tested whether the clustering bias was altered by the administration of oxytocin using simulations
272 similar to those used in Figures 2D-H. The clustering bias between generated spines observed in
273 VPA-exposed animals during saline administration was reduced by nasal oxytocin administration
274 (Figures 5D-F, J, and S4). By contrast, oxytocin had a less pronounced effect on the proximity
275 between eliminated spines (Figures S3B, 5G-I, 5J, and S4). We next analyzed the effect of
276 oxytocin on axons. The bouton density, generation, and elimination of each axon species were
277 not significantly different before and after oxytocin administration (Figure S6).
278
279 **Gene expression analysis in adult ASD model marmosets**
280 To explore the molecular mechanisms of altered spine dynamics in VPA-exposed marmosets and
281 to assess the validity of adult VPA-exposed marmosets as a model of idiopathic ASD, we
282 performed transcriptome analysis of the cerebral cortex using custom-made marmoset
283 microarrays. Among the 9,296 genes expressed in cortical tissues, there were 2,484 differentially
284 expressed genes (DEGs) with an adjusted *P*-value for multiple comparison (P_{adj}) of < 0.05. First,
285 we compared the DEGs in the cortical regions associated with social behavior between VPA-
286 exposed marmosets and the postmortem brains of humans with ASD [51], and found a significant
287 positive correlation between the two groups [52] (Figure 6A). This was similar to our previously
288 reported similarity between juvenile VPA-exposed marmosets and humans with ASD [22]. In
289 addition, the modulation of gene expression in adult marmoset models and in human ASD was
290 compared in each gene module that was previously configured by weighted gene co-expression
291 network analysis (WGCNA) for samples from typically developed humans and those with ASD
292 [22, 52]. In both the marmoset model and human ASD, the majority of genes in modules associated
293 with neurons and oligodendrocytes were downregulated (Figure 6B), while genes in modules
294 associated with astrocytes and microglia were upregulated (Figure 6B). The direction of gene

295 expression modulation of adult VPA-exposed marmosets was very similar to that of human ASD
296 samples in 10 modules, compared to nine modules for juvenile VPA-exposed animals [22] (Figure
297 6C). The high similarity between VPA-exposed marmosets and human ASD contrasted with
298 representative rodent monogenetic ASD models, which replicated human modulations only in
299 limited gene modules and cell types (Figure 6C). One explanation for this may be that these
300 transgenic mice are a model of a specific type of ASD in which one gene contributes particularly
301 strongly, which is not the case in idiopathic ASD.
302
303 We also analyzed DEGs in each cell type. This analysis confirmed the presence of a VPA-
304 exposed marmoset-specific phenotype across the four cell types, as well as in vascular endothelial
305 cells in the brain (Figure 6D). Pathway analysis of cell type-specific DEGs showed pathway
306 abnormalities in each of these cell types. For example, microglial modules exhibited
307 abnormalities associated with inflammation, which fits well with the inflammation hypothesis of
308 ASD [53].
309

310 **Discussion**

311 In this study, we used in vivo two-photon microscopy to monitor neurite dynamics in the apical
312 tuft dendrites of dmPFC layer-2/3 pyramidal neurons and adjacent axons in VPA-exposed
313 marmosets. The main findings were as follows. First, new spines were generated in clusters and
314 subsequently carried over much more frequently than non-clustered spines. Second, turnover rates
315 of both dendritic spines and presynaptic boutons were higher than in control animals. Specifically,
316 bouton turnover in VPA-exposed marmosets was significantly greater in local axons, but not in
317 callosal axons, compared to controls, indicating possible maladjustment of projection-specific
318 circuit plasticity. Finally, nasal administration of oxytocin to model marmosets reduced the
319 tendency of spines to cluster without affecting their turnover rate. These spine-associated effects
320 of oxytocin support its therapeutic potential in individuals with ASD.

321

322 The process by which coactivating spines were formed in close proximity to each other during
323 operant tasks was elucidated using a combination of behavioral tasks and functional two-photon
324 imaging [5]. Moreover, in layer-2/3 pyramidal neuron dendrites of the ferret visual cortex,
325 neighboring spines tend to have similar visual representations [54]. These and other reports suggest
326 a link between the proximity of the distance between generated spines and similarities in their
327 reactivity. In fact, electron microscopy studies have shown that adjacent spines often serve as
328 postsynaptic targets for single axons [55]. Clustered emergent spines that receive structurally or
329 functionally similar inputs are thought to enable nonlinear dendritic computation and may
330 facilitate the ability to acquire memory and behavioral skills through learning and experience [11,
331 12, 14-17, 56]. Alternatively, clustered generated spines may also help stabilize formed circuits and
332 accelerate learning due to their redundant involvement in the circuit [57]. In fact, *CCR5* KO and
333 *MeCP2* duplication mice commonly show elevated spine turnover and clustering as well as high
334 learning efficiency [10, 18]. On the other hand, over-efficient formation of neural circuits due to
335 excessive synaptic clustering may result in the preservation of synapses that should be removed
336 and may prevent the formation of additional neural circuits. Consistent with this hypothesis, VPA-
337 exposed marmosets learned faster than UE marmosets during the first discrimination phase of a
338 spatial reversal learning task, but learned slower after paradigm reversal [58].

339

340 Previous in vivo two-photon microscopy studies of ASD model mice have shown a common
341 phenotype of high spine turnover in the motor and early sensory cortices that are less associated
342 with ASD core symptoms than in the PFC [7-10]. Accumulating evidence, including the results of
343 this study, suggests that ASD-related genes and environmental factors converge across species,
344 resulting in a phenotype of increased spine dynamics that continuously promotes neural circuit
345 remodeling. Compared to spine turnover (generation and elimination), spine clustering in ASD
346 animal models has been reported very infrequently to date, and only in the motor and visual

347 cortices in *MeCP2* duplication models [10]. Compared to VPA-exposed marmosets, the degree of
348 clustered emergence in *MeCP2* duplication mice appears to be substantially lower. The reasons
349 for this discrepancy are currently unclear. However, it may be due to differences in spine density,
350 plasticity molecules, or subcellular organelles between species, cortical areas, syndromic and
351 idiopathic ASD models, and deep and upper-layer pyramidal neurons. In any case, the strong
352 clustering tendency in the dmPFC of VPA-exposed marmosets underscores the importance of
353 clustering in the pathogenesis of idiopathic ASD and warrants further research of clustered spine
354 emergence in both physiological and pathophysiological conditions.
355
356 The synaptic connections of local neural circuits exhibited more plasticity in VPA-exposed
357 animals than in UE animals, whereas the long-distance callosal neural circuits did not show
358 plasticity differences. This suggests that projection-specific plasticity control may be altered in
359 ASD [37, 38, 59]. The excessive plasticity in the local neuronal circuits of VPA-exposed marmosets is
360 reminiscent of the enhanced long-term potentiation of layer-5 pyramidal neurons in acute slice
361 preparations in a VPA-exposed rat ASD model [60]. However, differences in synaptic remodeling
362 of different types of cortical inputs have never been compared in living animals or in vitro in ASD
363 models. Postsynaptic neuron-specific deletion of the *Fmr1* gene in mice reduced the amplitude of
364 synaptic transmission in callosal inputs but not in local inputs, suggesting the existence of
365 differential regulation between the group of inputs [61]. Several experiments, including single-cell
366 transcriptome analyses, have shown a variable number of DEGs between cortical layer-specific
367 excitatory neurons[62] or between cortical areas [51, 63] in human ASD. These differences may serve
368 as the basis for projection-specific circuit plasticity. Abnormalities in brain connectivity strength
369 between ASD-relevant brain regions in humans with ASD have been demonstrated by functional
370 brain imaging techniques such as functional magnetic resonance imaging (fMRI) and
371 magnetoencephalography (MEG) /electroencephalography (EEG), using the degree of brain
372 activity coherence as an indicator [1, 38, 40]. Differences in the degree of bouton dynamics between

373 local and callosal connections in VPA-exposed marmosets suggest that in addition to variations
374 in connection strength, changes in projection-specific synaptic remodeling may also contribute to
375 ASD symptoms. It will be interesting to analyze whether mismatches in plasticity control
376 involving local and long-range connections facilitate autonomous local circuit remodeling
377 independent of the highly contextualized information computed in the brain-wide global network.
378
379 To identify therapeutic targets, it will be valuable to determine the molecular mechanisms that
380 govern spine turnover and spine clustering in VPA-exposed marmosets [64]. Our study
381 demonstrated that oxytocin reduced clustering of generated spines in ASD model marmosets
382 without altering spine turnover, while in mice the effect of oxytocin on synaptic plasticity has
383 been studied in various brain regions such as the olfactory system, hypothalamus, and neocortex
384 [42, 65]. In the present study, we have substantiated the presence of the oxytocin receptor protein
385 through Western blot analysis within the synaptosomal fraction isolated from the gray matter of
386 the adult marmoset prefrontal cortex (Figure S5). This observation implies that chronic oxytocin
387 exposure potentially exerts a direct inhibitory influence on spine clustering by modulating
388 intracellular signaling pathways, notably the MAPK/ERK pathway, downstream of oxytocin
389 receptor activation. Oxytocin receptors in marmosets are notably expressed in the basal ganglia
390 of the nucleus basalis of Meynert (NBM), a prominent cholinergic region within the brain. The
391 NBM serves as a significant source of cholinergic innervation to various brain regions, including
392 the neocortex, and plays a pivotal role in regulating selective attention and motivational
393 processes[50]. It is plausible that the alteration of spine clustering induced by oxytocin may involve
394 the modulation of cholinergic inputs. Oxytocin's inhibitory effect on spine clustering could
395 restrain excessively prolonged circuit stability and mitigate behavioral perseverance, as reported
396 in human ASD [66]. Differences in oxytocin systems between rodents and primates may
397 significantly affect therapeutic efficiency, which underscores the importance of primates in
398 translational research on oxytocin [50]. Spine clustering in the *MeCP2* duplication mouse model

399 was suppressed by an inhibitor of Ras-MAPK(ERK) signaling without altering the spine
400 generation rate [67]. Ras, like other proteins such as Rho, Rac, and cofilin, has been reported to
401 diffuse from activated spines to neighboring spines via dendrites and is thought to alter the
402 plasticity of neighboring spines [5, 31, 32, 68]. Interestingly, transcriptome analysis of our model
403 marmosets showed four times greater upregulation of *TGF-β2*, which is upstream of the Ras-
404 MAPK pathway, than control marmosets. Synaptic plasticity involves not only neurons but also
405 diverse glial cells. We found that microglia demonstrated activation of signals related to viral
406 infection, inflammation, and reorganization of the actin cytoskeleton (Figure 6D). Suppression of
407 excessive microglial activation with minocycline or other matrix metalloproteinase-9 inhibitors
408 has been reported to suppress excessive spine turnover in fragile X model mice [8]. Our
409 transcriptomic analysis also revealed significant downregulation of myelin-related genes, such as
410 PLP1, which suppresses heightened cortical plasticity. On the other hand, it has been shown that
411 the stress hormone corticosterone increases spine turnover in mice [69]. Indeed, as in mouse ASD
412 strains [70] and humans with ASD [71], our ASD model marmosets have aberrant cortisol responses
413 [72], suggesting that environmental factors such as anxiety and endocrine system disorders may be
414 responsible for the increase in synaptic remodeling. Therefore, oxytocin, which reduces spine
415 clustering, could be beneficial for individuals with ASD when combined with the suppression of
416 spine turnover.

417 **Limitations of the study**

418 In this study we did not investigate inhibitory synapses. The location of inhibitory inputs and the
419 local balance between excitatory and inhibitory inputs may also have a significant effect on
420 nonlinear information integration by dendrites. We were also unable to analyze the genetic,
421 anatomical, or electrophysiological characteristics of the pyramidal neurons that we examined.
422 Activity-dependent labeling of neurons would allow for better characterization of the relationship
423 between neuronal activity and spine clustering. Electron microscopy analysis of clustered
424 generated spines would have made it possible to confirm the presence of common presynaptic

partners. We believe that the future implementation of these approaches will better clarify the nature of spine clustering in autism models.

Acknowledgments

We thank H. Kasai of The University of Tokyo for helpful discussion and suggestions about two-photon imaging, and both H. Yamasue of Hamamatsu University School of Medicine and T. Minamimoto of QST Japan for their careful reading and thoughtful comments on the manuscript. We are also grateful to T. Araki, S. Wakatsuki and M. Iwasaki of the National Center of Neurology and Psychiatry (NCNP) for helpful discussion about experiments and marmoset surgery. We also thank A. Tsuchiya, M. Nakamura, T. Sato, W. Suzuki, A. Mishima, K. Mimura, and N. Miyakawa of our lab for supporting primate experiments, and R. Saito, Y. Katakai, and other members of the NCNP primate facility for caring for VPA-exposed and UE marmosets. A. Sawatari and S. Ikeda of Iwate University assisted with spine volume analysis. English editing was performed by Zenis, co. Ltd., Kyoto, Japan. This work was supported by Intramural Research Grants for Neurological and Psychiatric Disorders from the NCNP (3-5, J.N.; 29-6, N.I.), a Novartis Research Grant 2019 (S.W.), JSPS KAKENHI Grant Numbers JP18K06497 and JP22K07363 (J.N.), and AMED Grant Number JP21dm0207066 (N.I.).

Author contributions

J.N. and N.I. designed the study; J.N., S.W., R.I., and K.S. performed the in vivo two-photon imaging; K.N. generated the autism model marmosets; J.N. and R.I. conducted image analyses; E.S., H.T., H.M., A.W., and T.Y. prepared the AAV vectors.; S.W., T.O., K.S., K.H., K.S., and I.M. conducted the microarray analysis.; K.S. and R.I. performed immunohistochemistry; and J.N. and N.I. wrote the manuscript. All authors approved the final version of the manuscript. Correspondence and requests for data should be addressed to J.N. or N.I.

Declaration of interests

The authors declare no competing interests.

Inclusion and diversity

We support inclusive, diverse, and equitable research conduct.

METHODS

Animals

All experimental procedures were approved by the Animal Research Committee of the National Center of Neurology and Psychiatry. Common marmosets (*Callithrix jacchus*) were housed in captivity at the National Center of Neurology and Psychiatry under a 12-h/12-h light/dark cycle and were fed food (CMS-1; Clare Japan) and water ad libitum. Temperature was maintained at 27-30°C and humidity at 40-50%.

Marmoset ASD model

Serum progesterone levels in female marmosets were regularly measured to determine the date of fertilization. Four percent VPA dissolved in 10% glucose solution was administered intragastrically to pregnant marmosets at 200 mg/kg/day daily for 7 days starting on gestation day 60. No doses were given to control mothers. The obtained ASD model offspring from VPA-administered mothers and control offspring from UE mothers were kept in their home cages until the day of inoculation with AAV vector. We used four UE marmosets (monkeys KR (f, 1.3), TR (f, 3.2), VR (m, 2.2), and BH (m, 1.3)) and three VPA-exposed marmosets (monkeys PR (f, 1.5), SH (f, 1.4), and MS (m, 1.3)); f or m and numbers in parentheses indicate sex and age in years at the time of AAV inoculation, respectively.

AAV vector inoculation of the marmoset neocortex

477 Each experimental marmoset was pretreated with the antibiotic cefovecin sodium (8 mg/kg body
478 weight, intramuscular (i.m.); Zoetis), prednisolone (2 mg/kg body weight; i.m.), the analgesic
479 ketoprofen (2 mg/kg body weight, i.m.), and atropine (0.15 mg/kg body weight, i.m.). It was then
480 anesthetized with ketamine (15 mg/kg body weight, i.m.; Daiichi-Sankyo) and xylazine (1.2
481 mg/kg body weight, i.m.; Bayer), which were supplemented with sevoflurane inhalation (2-4%).
482 The marmoset was then fixed to a stereotaxic instrument (SR-6C-HT; Narishige, Tokyo, Japan).
483 During all surgical procedures, marmosets were also supplied with humidified oxygen as needed,
484 and warmed to 37-39 °C with a heating pad (FST-HPS; Fine Science Tools, North Vancouver,
485 Canada). Body temperature, SpO_2, heart rate, cardiac electrogram, respiratory rate, and actual
486 concentration of oxygen and sevoflurane were measured using a biomonitor (BSM-5132;
487 Nihonkoden, Tokyo). After incision of the skin at the midline, the skull was exposed and a 1-mm-
488 diameter hole was made bilaterally above the PFC Brodmann area 8 (11.5 mm anterior to the
489 interaural line, 3 mm lateral to the midline) using a dental drill.
490
491 A puller (PC-100; Narishige) was used to create a micropipette (tip diameter 30-50 μm) from a
492 micro glass tube (1.0-mm diameter; TW100F-4; WPI, USA). The pulled micropipette was then
493 beveled using a micro grinder (EG-402; Narishige) and was sterilized by overnight exposure to
494 UV light or ethylene oxide. The pipette was set to a glass microsyringe (Model 1701,10 μL;
495 Hamilton, USA) using a Priming kit (55750-01; Hamilton), and the microsyringe was back-filled
496 with silicon oil and attached to a microsyringe pump (LEGATO 130; WPI) fixed to the
497 manipulator of a stereotaxic instrument (SM-15R; Narishige). The micropipette was then tip-
498 filled with AAV vector suspension and slowly inserted through the dura and into the neocortex,
499 avoiding large blood vessels. The total 0.5-μL volume of AAV vector was then inoculated at 0.1
500 μL/min at a depth of 0.8 mm from the surface. The viral preparations were adjusted to the
501 following final concentrations: 1×10^9 vg/mL for rAAV1-Thy1S-tTA and 1×10^{12} vg/mL for
502 AAV1-TRE3-tdTomato, expressing red fluorescence protein; 5×10^9 vg/mL for rAAV2/1-Thy1S-

503 tTA and 1×10^{12} vg/mL for rAAV2/1-TRE3-mClover, expressing green fluorescence protein.
504 After the 5-min incubation period, the micropipette was retracted, a silicon plug was stuffed into
505 the cranial hole, and the skin incision was closed with sutures. After recovery from anesthesia,
506 the marmoset was returned to its home cage.
507
508 **Imaging window preparation**
509 Each experimental marmoset was pretreated with the antibiotic cefovecin sodium, prednisolone,
510 the analgesic ketoprofen, and atropine. It was then anesthetized with ketamine and xylazine,
511 which were supplemented with sevoflurane inhalation (2-4%). The marmoset was then fixed to a
512 stereotaxic instrument. The marmoset was also supplied with humidified oxygen and warmed up
513 to 37-39 °C. After skin incision at the midline, the skull was exposed and a 4-mm-diameter hole
514 was made at the point where the AAV was inoculated using a dental drill fixed to a stereotaxic
515 manipulator (SM-15R; Narishige). The dura mater was carefully removed using microsurgical
516 ophthalmic scissors, fine forceps, and a microhook to minimize any pressure applied to the surface
517 of the brain. A piece of coverslip, consisting of three laminated circular coverslips (5-mm
518 diameter + 3-mm diameter × 2), was used to cover the exposed brain surface[26]. The coverslip was
519 fixed using dental acrylic (Fuji-Lute; GC Corp., Tokyo, Japan) to create an imaging window in
520 the skull. A custom-made stainless-steel recording chamber (ICM, Tsukuba, Japan) was then
521 attached to the skull using dental resin (Bistite II; Tokuyama Dental, Japan) such that the imaging
522 window was in the center of the chamber. After the imaging window was covered with an acrylic
523 lid, the marmoset was allowed to recover from the anesthesia in the monkey ICU room and was
524 then returned to its home cage.
525
526 **In vivo two-photon excitation microscopy**
527 In vivo two-photon imaging of neurites was performed using an upright microscope (BX61WI;
528 Olympus) equipped with a laser scanning microscope system (FV1000; Olympus) and a water-

529 immersion objective lens (XLPlanN, 25×, NA 1.05; Olympus). The system included mode-locked,
530 femtosecond-pulse Ti:sapphire lasers (MaiTai; Spectra Physics) set at a wavelength of 980 nm.
531
532 Imaging sessions were conducted every 3 days. A marmoset was pretreated with atropine and
533 anesthetized with sevoflurane inhalation (3-5%). The marmoset was laid in the prone position and
534 its head was fixed using the imaging chamber and brass posts (Figure 1A). In each case, the
535 imaging location was identified based on blood vessel morphology. Tuft dendritic branches (<
536 100 μm depth) of layer 2/3 pyramidal neurons were used for two-photon imaging experiments.
537 An objective lens correction collar was manually set just before imaging so as to minimize
538 spherical aberrations (i.e., to acquire the brightest image possible). The reciprocal scan mode was
539 used to scan each *xy*-image (256 by 256 pixels; 65 msec/frame). Three-dimensional fluorescent
540 images with 51 *xy*-images, each separated by 0.5 μm, were obtained at each imaging site.
541
542 **Dendritic spine and axonal bouton analysis**
543 We applied a 2-pixel spatial Gaussian filter and then registered the obtained *xyz*-images using the
544 StackReg or Multi-StackReg plug-in function of Image-J (Fiji)[73]. Spines were identified as
545 protrusions from dendrites with an apparent head structure. Filopodial protrusions (which have
546 no apparent spine head) were excluded from the analysis. Two spines observed during different
547 sessions were considered to represent the same spine if the initial position subsequently exhibited
548 the same distances from adjacent landmarks. A spine was interpreted as lost if it temporarily
549 disappeared. The minimum spine length was set at 0.4 μm. Snowman-shaped spines (shaped like
550 two spheres stuck together) were interpreted as two separate spines. Only spines that appeared
551 laterally were included in the analysis (this underestimated the spine density). Dendrites that were
552 visible in all sessions were used in the analysis.
553

554 We also analyzed the axons that appeared in the same images as the dendrites. For axon analysis,
555 we used five marmosets that expressed mClover in the right hemisphere and tdTomato in the left
556 hemisphere (UE monkeys: TR, VR, BH; VPA-exposed monkeys: SH, MS). We applied a 2-pixel
557 spatial Gaussian filter to the *xyz*-images and obtained *z*-substacked average images for a
558 predetermined z number for each axon. By combining images obtained at the optimal depths, we
559 created montage images for each axon, avoiding dendrites and other axons present at other
560 imaging depths. We then examined the brightness along the axon shaft using the Plot-profile
561 function of Image-J[73]. The ratio of bouton brightness to neighboring axon shaft brightness was
562 then calculated. We did not see axons that were much thicker than the diffraction limit of our two-
563 photon imaging, and discarded areas that overlapped with other dendrites and axons. Boutons
564 were detected as bright swellings along axons, with intensity values at least two-fold higher than
565 that of the flanking axon backbone [74]. Since we could not detect axonal synapses below the bouton
566 threshold, the subthreshold boutons may have been misidentified as newly generated boutons
567 when they enlarged and therefore exceeded the threshold in the next imaging session. As a
568 consequence, the number of newly generated boutons may have been overestimated. Likewise,
569 the number of boutons that were eliminated may also have been overestimated. This may explain
570 the result that the overall bouton turnover was higher than the spine turnover. The 3-day bouton
571 generation and elimination for unit axon length were obtained by dividing the number of boutons
572 generated and eliminated over a 3-day period by the axon length. The 3-day bouton generation
573 and elimination as a percentage were calculated by dividing the 3-day bouton generation and
574 elimination for unit axon length by the mean bouton density. We did not exclude varicosities of
575 transfer vesicles. In the next session, boutons located within 1 μm of the expected point were
576 interpreted as identical to those in the previous session.
577
578 The percentage of newly formed spines or boutons was calculated as the number present at time
579 point 2 but not at time point 1, divided by the total number present at time point 1 and multiplied

580 by 100. The percentage of eliminated spines or boutons was calculated as the number present at
581 time point 1 but not at time point 2, divided by the total number present at time point 1 and
582 multiplied by 100.
583
584 **Monte Carlo simulation of newly generated or eliminated dendritic spines**
585 To obtain unbiased distributions of the inter-spine distance of newly generated or eliminated
586 spines, each dendrite was concatenated in random order, producing one long dendrite repeatedly
587 (1,000 times permutation; Figures 2C and S3C, D). The average clustering probability was then
588 calculated. We set the clustering threshold at 3 μm since several biochemical, physiological, and
589 structural studies have suggested that a 3 to 10 μm distance between spines facilitates sharing of
590 resources, spine co-activation, and learning-induced structural plasticity [30-36]. In Fig. S2A, the
591 threshold applied for the analyses (3 μm) was confirmed to be appropriate because it is located at
592 the lowest end of the plateau [10]. Monte Carlo simulation was performed to determine whether a
593 clustering bias existed in the process of spine generation or elimination [18]. The simulation used
594 the total dendrite length and the total number of generated and eliminated spines. The positions
595 of generated and eliminated spines on the dendrites were then regenerated with a uniform random
596 distribution using Excel software. The distances between generated and eliminated spines were
597 computed for all dendrites and the percentage of clustered events was calculated (Figure 2D). As
598 clustered spines may appear more on specific dendrites, another simulation was conducted on
599 individual dendrites without connecting each dendrite, and similar results were obtained (Figure
600 S2D-H). The above simulations were performed with 100,000 iterations to obtain the distribution
601 of clustering events, and the results are shown in Figures 2E-H, 5D-I, S2E-H, and S4A-F by
602 connected gray lines.
603
604 **Dendritic spine volume measurement**

605 We calculated the spine-head volume by partially summing the fluorescence values of five
606 sequential *z*-images by taking the moving average of the image stack along the *z*-plane. This was
607 done to avoid summing other dendrites or axonal fibers present in different imaging planes.
608 Because the thickness of dendritic spines is near the diffraction limit of a two-photon microscope,
609 partially summed values (2 μm range in the *z*-direction) can be used to reflect spine volumes.
610 Thus, the maximum value of *z*-moving average images allowed us to obtain good approximations
611 of the total *z*-summed stacked images. The normalized spine volume was obtained by dividing
612 the spine fluorescence intensity by the fluorescence intensity of the adjacent dendrite shaft.
613

614 **Nasal oxytocin administration to VPA-exposed marmosets**

615 New World monkey oxytocin (Pro-8 oxytocin [75]) was custom synthesized (GenScript,
616 Piscataway, NJ, USA) and was dissolved in 0.5 mg/mL of 0.9% NaCl solution. The oxytocin
617 solution was typically administered 2.5 h before the two-photon imaging and at approximately
618 same time on days without two-photon imaging. Oxytocin solution was applied to the nasal
619 cavities of each marmoset at a dose of 150 μg/kg body weight as in a previous study[75], using a
620 micropipette equipped with a soft silicon tube on the tip. Oxytocin was administered every day
621 (monkey MS) or every other day (monkeys PR and SH) starting on day−4 (Figure 5A).
622 Verification of oxytocin delivery to the cerebral interstitial fluid was verified by measuring the
623 plasma Pro8-oxytocin concentration using a sandwich competitive chemiluminescent enzyme
624 immunoassay (CLEIA) (ASKA Pharma Medical, Fujisawa, Japan). The Pro8-oxytocin
625 concentration in all blood samples was monotonically increased 30 min after nasal oxytocin
626 administration (mean ± s.d. = 30.6 ± 14.8 pg/mL; n = 2 males and 3 females) but not 30 min after
627 nasal saline administration (mean ± s.d. = 9.9 ± 1.7 pg/mL; n = 2 males and 3 females); thus, we
628 concluded that Pro8-oxytocin was successfully delivered to the interstitial fluid of the neocortex.
629

630 **Microarray gene expression analysis**

631 Microarray analysis of marmoset gene expression was performed using brain samples from three
632 adult VPA-exposed and three UE marmosets, as previously described[22]. To increase data
633 reliability, we pooled the data from the social brain areas (area 12 and area TE) that are affected
634 in humans with ASD. Tissue sampling and GeneChip analysis were conducted as previously
635 reported[22]. Briefly, marmosets were anesthetized with ketamine hydrochloride (50 mg/kg, i.m.)
636 and sodium pentobarbital (90-230 mg/kg, intraperitoneal; Kyoritsu Seiyaku). After reflections
637 had completely disappeared, the animals were transcardially perfused with diethyl pyrocarbonate-
638 treated phosphate-buffered saline, and the cortical tissue was isolated and immersed in RNAlater
639 (Thermo Fisher Scientific). Total RNA was extracted using the RNeasy Mini Kit (Qiagen, Hilden,
640 Germany). RNA integrity was assessed using a Bioanalyzer (Agilent Technologies), and samples
641 with RNA integrity number values >7 were evaluated. Biotin-labeled cRNA probes were prepared
642 using the GeneChip 3'IVT Express Kit (Affymetrix). The probes were hybridized to a custom-
643 made microarray (Marmo2a520631F) using the GeneChip Hybridization, Wash, and Stain Kit
644 (Affymetrix). Microarrays were scanned using a GeneChip Scanner 3000 (Affymetrix) and
645 processed using MAS5, and the reliability of probe detection was examined. Data were
646 normalized using GCRMA. Genes with log2 expression values greater than 5 were considered to
647 be expressed in brain tissue. The log fold-change (logFC) value was used as a measure of gene
648 expression modulation and evaluated using Welch's t-test with Benjamini-Hochberg adjustment
649 (P_{adj}). For affected genes with multiple probes, the data from the probe with the lowest P_{adj} was
650 used. To compare gene expression modulations in the marmoset model with those in human ASD
651 postmortem samples [51] commonly modulated genes with $P_{adj} < 0.1$ were used.
652
653 **Comparison of log fold change (logFC) values between human ASD and animal models, as**
654 **determined by gene co-expression modules.**
655 To compare gene expression changes between the ASD group and the typically developed human
656 group, or between the ASD model animals and controls, logFC values were calculated for the

genes analyzed by the gene chip. The concordance values were then calculated for each gene module [51, 52] to show consistency in the direction of gene expression changes between human ASD and the animal models (Figure 6C). The concordance value was the percentage of genes that changed in a common direction (first and third quadrants in Figure 6B) in human ASD and the model animal. For modules with at least eight common genes between the animal model and human ASD, the concordance values are shown in color in Figure 6C. The logFC values of VPA rats[76] (age 35 days), BTBR mice [77] (age 4 months), *Fmr1* KO mice[78] (age 8-14 weeks), *MeCP2* heterozygous mice [79] (age 5 weeks), *Tcf4*$^{tr/+}$ mice [80] (age 60-80 days), 15q13.3 deletion mice [81] (age 10-22 weeks), and *Pten*^{m3m4} mice [82] (age 6 weeks) were obtained from previously published studies. To compare gene expression modulations in the marmoset model with those in postmortem samples of humans with ASD [51], commonly modulated genes with $P_{adj} < 0.1$ were used. For the rat VPA models and BTBR mice, genes with $P_{adj} < 0.05$ were selected; for other models and human ASD, genes with $P_{adj} < 0.1$ were selected. To compare gene expression modulations in the rodent models with those in human ASD, gene symbols were converted using HomoloGene (NCBI, https:// www.ncbi.nlm.nih.gov/homologene, release 68). Due to the small number of genes that are commonly affected, mouse models of maternal immune activation and *Shank3* knockout were not included in the list.

Signaling pathway estimation of marmoset genes

Pathway analysis of marmoset genes was conducted using IPA software (Qiagen, Summer Release 2020). Genes specific to brain cell types (neurons, astrocytes, microglia, oligodendrocytes, and endothelial cells) were selected from genes with mean logFC gene enrichment values > 2, among the top-ranked cell type-enriched genes based on the human single-cell analysis data in a previous report [83].

Examination of glial cell activation

683 Marmoset brains fixed in 4% PFA were replaced with 30% sucrose in 0.1 M phosphate buffer
684 (pH 7.4). Frozen sections with 50 μm thickness were prepared using a microtome (Retoratome
685 REM-710; Yamato-Kohki, Saitama, Japan). Brain slices were treated in antigen-retrieval solution
686 (HistoVT One; Nacalai Tesque, Kyoto, Japan) at 70°C for 20 min, followed by PBS washing and
687 blocking (blocking buffer: 5% normal goat serum, 0.4% TritonX-100 in PBS) at room
688 temperature for 60 min. After blocking, free-floating brain slices were incubated in a solution of
689 anti-Iba1 antibody (1:2000; Fuji film-Wako) or anti-GFAP antibody (1:10,000; Agilent-Dako) at
690 4°C overnight. The slices were washed with PBS (10 min, three times) and incubated with biotin-
691 labeled goat anti-rabbit secondary antibody (1:500; Vector Labs) at room temperature for 90 min.
692 The slices were washed with PBS (10 min, three times), then reacted with the ABC complex for
693 90 min at room temperature (Vectastain Elite ABC kit; Vector Labs). After washing with
694 phosphate buffer (10 min, three times), the slices were mixed with nickel-sensitized DAB reaction
695 solution (0.01% 3,3'-diaminobenzidine-4HCl) to develop color. The samples were washed with
696 phosphate buffer, mounted on glass slides, and dehydrated with ethanol and xylene. The glass
697 slides were then sealed with coverslips for microscopic observation. Microglia and astrocytes
698 were observed and cell numbers were counted using a Neurolucida 360 system equipped with an
699 inverted microscope (MBF Bioscience, Williston, VT, USA).
700
701 **Western blotting**
702 Three adult UE marmosets (female, 2.8 year-old; male, 6.8 y; female, 8.8 y) were deeply
703 anesthetized with pentobarbital after ketamine preanesthesia. After confirming the disappearance
704 of reflexes, ice-cold PBS was transcardially perfused and subsequent cardiac arrest was
705 confirmed. While continuing ice-cold PBS perfusion, a portion of the skull was removed and the
706 entire brain was harvested. The gray matter of the prefrontal cortex was excised from the brain
707 and placed in a 2-mL plastic tube, which was immediately frozen on dry ice and stored at –80°C
708 until use. 53-93 mg of frozen prefrontal gray matter was placed in a Lysing Matrix D 2-mL tube

709 (MP-Biomedicals, Irvine, CA, USA) cooled on ice, 800 μl of Syn-PER™ Synaptic Protein
710 Extraction Reagent (Thermo Fisher Scientific, Waltham, MA, USA) and cOmplete mini Protease
711 Inhibitor Cocktails (Merck, Darmstadt, Germany) was added. The tissue was homogenized by
712 shaking the Matrix D tube at 3,200 rpm for 30 seconds using a bead beater homogenizer (μT-12,
713 Taitec, Koshigaya, Japan). The homogenate was then centrifuged at 1200 g for 10 min. The
714 supernatant was further centrifuged at 15,000 g for 20 min to obtain a synaptosome fraction. The
715 synaptosome fraction was re-suspended in 700 μl of SynPER and the protein components of the
716 synaptosome were extracted by mixing 70 μl of 100% Trichloroacetic acid and allowing it to
717 stand for 30 min on ice. The protein extract was collected by a centrifugation at 15,000 g for 5
718 min. SDS-PAGE sample buffer was then added to the extract and neutralized by adding 1 M Tris.
719 SDS-PAGE (7.5% gel, 10 or 1 μg total protein per lane, for anti-oxytocin-receptor or anti-
720 PSD95/anti-β-actin, respectively) was performed and proteins were transferred to PVDF
721 membranes and stained with 0.2% Ponceau-S in 5% acetic acid. The membrane was then
722 incubated in a blocking solution containing 5% skimmed milk, 0.2% Tween20, and 0.02% NaN_3
723 in PBS at 4°C, overnight. Membranes were incubated with the following primary antibodies: anti-
724 PSD95, mouse, Novus Biologicals, #NB300-556, 1:4,000; anti-Oxytocin receptor, rabbit, Abcam,
725 #217212, 1:100; anti-β-actin, mouse, Santa Cruz, #sc-47778, 1:4,000 in PBS-T (0.1% Tween20
726 in PBS) for 3.5h at room temperature. After twice of washing with PBS-T, the membranes were
727 treated with secondary antibodies: Sheep anti-mouse IgG +HRP, Cytiva, #NIF825, 1:4,000; Goat
728 anti-rabbit IgG +HRP, MBL, #458, 1:5,000 for 30 min at room temperature. After 4 washes with
729 PBS-T, the blots were visualized with ECL Western Blotting Reagents, Cytiva, #RPN2109, and
730 detected using Fusion-S solo imager (Vilber, Collégien, France).
731
732 **Statistical analysis**
733 All data are presented as mean ± s.e.m (*n* = dendrite or axon numbers) unless otherwise stated.
734 The Mann-Whitney rank sum test was used to analyze the data shown in Figures. 1C, 1D, 2B, 3E,

735 4D and Figure S1. The difference in probability distribution between cumulative plots was
736 calculated using the Kolmogorov-Smirnov test, as shown in Figures 1E, 1F, 2C, and 4E. The
737 differences between means were analyzed using the Friedman test, as shown in Figures 5B, 5C,
738 Figures S3A, S3B and the Kruskal-Wallis test in Figures S6A-F. The Fisher's exact test was used
739 to examine the frequency of the carryover spines and that of the total spines in Figure 3C and 3D
740 and to examine the spine survival rates for each condition in Figures 1G and 3F. The *P*-values in
741 Figure 5J were obtained from the distribution of the simulation. The *r* and *P*-values in Figures 6A
742 show Pearson's correlation coefficients (*r*) and their *P*-values (P_r) against zero. The concordance
743 values (*c*) and their *P*-values (P_c) in Figure 6B show the number of genes exhibiting concordant
744 changes between the animal model and human ASD divided by the total number of genes, and
745 the probability was calculated using the one-sided binomial test. Other statistical tests are
746 specified in the text or figure legends or elsewhere in the **Methods** section. Quantification,
747 simulation, and statistical analysis were performed using Microsoft Excel, GraphPad Prism 9.3.1.,
748 and Real Statistics software (for Kolmogorov-Smirnov test; www.real-statistics.com.). Analyses
749 on spines were first conducted by an analyst blinded to the sample labels and subsequently
750 validated by an independent analyst. In the context of axonal analysis, the quantification of
751 fluorescence intensity was carried out in a semi-automated manner, delineating a linear region of
752 interest (ROI) along the axon, utilizing Image-J (FIJI) software.
753
754 **Data availability**
755 The microarray data generated in this study have been deposited at NCBI GEO under accession
756 number GSE199560.
757
758 **Supplemental information**
759 **Figure S1. Glial cell activation after the final imaging session was negligible.** (**A**) Activated
760 astrocyte marker GFAP postive cell density was calculated in the fixed brain slices prepared

761 after the final imaging session. Distinct sign of astrocyte activation under the imaging window
762 was not detected (P = 0.26 at 83-115 mm cortical depth; Mann-Whitney U-test; Total 12 sites
763 on the dorsomedial prefrontal cortex (1.1×10^{-3} mm^3 for one site) from three marmosets). (**B**)
764 Microglia marker Iba-1 postive cell density was calculated as in (A). Obvious sign of microglia
765 activation under the imaging window was not detected. (P = 0.27 at 92-112 mm cortical depth;
766 Mann-Whitney U-test; Total 12 sites (1.1×10^{-3} mm^3 for one site) from three marmosets). Data
767 are represented as mean ± s.e.m.
768
769 **Figure S2. Examination of the proximity of dendritic spine generation.** (**A**) The relationship
770 between the clustering thresholds and differences in clustering probabilities of the newly
771 generated spines between VPA-exposed animals and UE animals. The threshold value applied
772 for the subsequent analyses (3 μm) was located at the lowest end of the plateau. (Related to Fig.
773 2). See Materials and Methods for details. (**B**) The clustered spine generation observed in the PFC
774 of marmoset model and in the motor cortex of a mouse syndromic autism model (*MeCP2*-
775 duplication) reported in previous literature[10]. In the graph, the clustering threshold (T_h) was set to
776 9 μm, which was common to both mouse and marmoset data (mean ± s.e.m.; n = 14 and 12
777 dendrites in four and three UE and VPA-exposed marmosets respectively). Note that the data for
778 mice is after four days of motor training. (**C**) The carryover spines in the marmoset PFC and those
779 in motor cortex in the MeCP2-dup mice. (**D**) Validation of clustering bias by another Monte Carlo
780 simulation. The new spine positions were randomly determined with a uniform distribution. This
781 was done without pooling the spine count and dendrite length of each dendrite in this simulation,
782 since the generation or elimination of spines may occur in specific active dendrites. Clustering
783 probabilities for all inter-spine distances were calculated for each simulation, and the distributions
784 of the clustering probability from 100,000 iterations are shown in (E)-(H). (**E-H**) Circles
785 connected with gray lines represent probability plots of clustering events from 100,000
786 simulations; the actual numbers of spine clusters are represented by arrows (P = 0.33 and 0.0062;

787 n = 23 and 65 newly generated spine pairs in 14 and 12 dendrites in UE and VPA-exposed animals,
788 respectively) (P = 0.083 and 0.46; n = 43 and 78 newly eliminated spine pairs in 14 and 12
789 dendrites in UE and VPA-exposed animals, respectively). Dotted red lines show 95th percentiles.
790 ***P < 0.001; **P < 0.01; *P < 0.05; n.s., not significant.
791
792 **Figure S3. Oxytocin did not modify the proximity of spine elimination in the model**
793 **marmosets.** (**A** and **B**) Mean values of 3-day total spine elimination (A) and clustered or non-
794 clustered spine elimination(B) are shown as in Fig. 5B, C. There were no significant changes after
795 oxytocin administration in either total spine elimination (A)(mean ± s.e.m.; P = 0.92, Friedman
796 test; n = 12 dendrites in three VPA-exposed animals) or clustered/non-clustered spine elimination
797 (B)(mean ± s.e.m.; P = 0.42 and P = 0.28 for clustered and non-clustered spine elimination,
798 respectively, Friedman test; n = 12 dendrites in three VPA-exposed animals). (**C** and **D**)
799 Distributions of inter-spine distances between newly generated spines (P > 0.85; Kolmogorov-
800 Smirnov test; n = 45, 43 and 39 spine pairs for D0-3, D3-6, and D6-9, respectively) or between
801 newly eliminated spines (P > 0.56; Kolmogorov-Smirnov test; n = 48, 38 and 48 spine pairs for
802 D0-3, D3-6, and D6-9, respectively). n.s., not significant.
803
804 **Figure S4. Oxytocin modifies the proximity of spine generation in the model marmosets.**
805 (**A**-**F**) Validation of clustering bias by another Monte Carlo simulation. In this simulation, the
806 new spine positions were randomly determined with a uniform distribution without changing
807 the spine number or length and number of each dendrite (See Fig. S2). Effects of oxytocin on
808 clustering bias of newly generated (A-C) and eliminated (D-F) spines. The graphs are shown as
809 in Fig. 5. (n = 32, 32, and 28 newly generated spine pairs and n = 34, 27, and 37 newly
810 eliminated spine pairs during the D0-3, D3-6, and D6-9 periods, respectively, in three VPA-
811 exposed animals). (**G**) The P-values expressed in logarithm from (A)-(F) are indicated. The red
812 dotted line indicates 0.05. **P < 0.01; n.s., not significant.

813

814 **Figure S5. Oxytocin receptors are present in the synapse of the marmoset's prefrontal**
815 **cortex gray matter.** Oxytocin receptors along with post-synaptic protein PSD95 and beta-actin
816 are detected using western blotting in the synaptosomal fraction derived from the prefrontal cortex
817 gray matter of three adult marmosets.

818

819 **Figure S6. Oxytocin does not significantly modify axonal bouton generation or elimination.**
820 (**A** and **B**) Mean bouton density values of ipsilateral (A) and contralateral (B) axons in VPA-
821 exposed animals are not significantly different before and after oxytocin administration. (mean ±
822 s.e.m.; $P = 0.997$ and $P = 0.90$ for ipsilateral and contralateral axons, respectively, Kruskal-Wallis
823 test; n = 17 and 21 for ipsilateral and contralateral axons, respectively) (**C** and **D**) Three-day
824 bouton generation (C) and elimination (D) during the D0-3, D3-6, and D6-9 periods for each axon
825 type are shown (mean ± s.e.m.; $P = 0.85$ and $P = 0.96$ for bouton generation and elimination,
826 respectively, Kruskal-Wallis test; n = 38 axons in two VPA-exposed animals). (**E** and **F**) Three-
827 day bouton generation (E) and elimination (F) during the D0-3, D3-6, and D6-9 periods for the
828 total axons in the VPA-exposed animals are shown as in (C) and (D) (mean ± s.e.m.; $P = 0.85$
829 and $P = 0.97$ for ipsilateral and contralateral bouton generation, respectively, $P = 0.99$ and $P =$
830 0.91 for ipsilateral and contralateral bouton elimination, respectively, Kruskal-Wallis test; $n = 17$
831 and 21 ipsilateral and contralateral axons in two VPA-exposed animals). n.s., not significant.
832 (Related to Fig. 5)

833

834

835

836 **References**

837 1. Geschwind, D.H. & Levitt, P. Autism spectrum disorders: developmental
838 disconnection syndromes. *Curr Opin Neurobiol* **17**, 103-111 (2007).

839 2. Bourgeron, T. From the genetic architecture to synaptic plasticity in autism
840 spectrum disorder. *Nat Rev Neurosci* **16**, 551-563 (2015).

841 3. Webb, S.J., Neuhaus, E. & Faja, S. Face perception and learning in autism
842 spectrum disorders. *Q J Exp Psychol (Hove)* **70**, 970-986 (2017).

843 4. Xu, T. *et al.* Rapid formation and selective stabilization of synapses for enduring
844 motor memories. *Nature* **462**, 915-919 (2009).

845 5. Hedrick, N.G. *et al.* Learning binds new inputs into functional synaptic clusters
846 via spinogenesis. *Nat Neurosci* **25**, 726-737 (2022).

847 6. Chen, J.L. & Nedivi, E. Neuronal structural remodeling: is it all about access?
848 *Curr Opin Neurobiol* **20**, 557-562 (2010).

849 7. Isshiki, M. *et al.* Enhanced synapse remodelling as a common phenotype in
850 mouse models of autism. *Nat Commun* **5**, 4742 (2014).

851 8. Nagaoka, A. *et al.* Abnormal intrinsic dynamics of dendritic spines in a fragile X
852 syndrome mouse model in vivo. *Sci Rep* **6**, 26651 (2016).

853 9. Pan, F., Aldridge, G.M., Greenough, W.T. & Gan, W.B. Dendritic spine
854 instability and insensitivity to modulation by sensory experience in a mouse
855 model of fragile X syndrome. *Proc Natl Acad Sci U S A* **107**, 17768-17773
856 (2010).

857 10. Ash, R.T., Park, J., Suter, B., Zoghbi, H.Y. & Smirnakis, S.M. Excessive
858 Formation and Stabilization of Dendritic Spine Clusters in the MECP2-
859 Duplication Syndrome Mouse Model of Autism. *eNeuro* **8** (2021).

860 11. Polsky, A., Mel, B.W. & Schiller, J. Computational subunits in thin dendrites of
861 pyramidal cells. *Nat Neurosci* **7**, 621-627 (2004).

862 12. Losonczy, A. & Magee, J.C. Integrative properties of radial oblique dendrites in
863 hippocampal CA1 pyramidal neurons. *Neuron* **50**, 291-307 (2006).

864 13. Makino, H. & Malinow, R. Compartmentalized versus global synaptic plasticity
865 on dendrites controlled by experience. *Neuron* **72**, 1001-1011 (2011).

866 14. Branco, T. & Hausser, M. Synaptic integration gradients in single cortical
867 pyramidal cell dendrites. *Neuron* **69**, 885-892 (2011).

868 15. Fu, M., Yu, X., Lu, J. & Zuo, Y. Repetitive motor learning induces coordinated
869 formation of clustered dendritic spines in vivo. *Nature* **483**, 92-95 (2012).

870 16. Stuart, G.J. & Spruston, N. Dendritic integration: 60 years of progress. *Nat*
871 *Neurosci* **18**, 1713-1721 (2015).

872 17. Kastellakis, G., Cai, D.J., Mednick, S.C., Silva, A.J. & Poirazi, P. Synaptic
873 clustering within dendrites: an emerging theory of memory formation. *Prog*
874 *Neurobiol* **126**, 19-35 (2015).

875 18. Frank, A.C. *et al.* Hotspots of dendritic spine turnover facilitate clustered spine
876 addition and learning and memory. *Nat Commun* **9**, 422 (2018).

877 19. Zhu, F. *et al.* Architecture of the Mouse Brain Synaptome. *Neuron* **99**, 781-799
878 e710 (2018).

879 20. Boroviak, T. *et al.* Single cell transcriptome analysis of human, marmoset and
880 mouse embryos reveals common and divergent features of preimplantation
881 development. *Development* **145** (2018).

882 21. Koopmans, F. *et al.* Comparative Hippocampal Synaptic Proteomes of Rodents
883 and Primates: Differences in Neuroplasticity-Related Proteins. *Front Mol*
884 *Neurosci* **11**, 364 (2018).

885 22. Watanabe, S. *et al.* Functional and molecular characterization of a non-human
886 primate model of autism spectrum disorder shows similarity with the human
887 disease. *Nat Commun* **12**, 5388 (2021).

888 23. Watanabe, T. *et al.* Diminished medial prefrontal activity behind autistic social
889 judgments of incongruent information. *PLoS One* **7**, e39561 (2012).

890 24. Penzes, P., Cahill, M.E., Jones, K.A., VanLeeuwen, J.E. & Woolfrey, K.M.
891 Dendritic spine pathology in neuropsychiatric disorders. *Nat Neurosci* **14**, 285-
892 293 (2011).

893 25. Mullins, C., Fishell, G. & Tsien, R.W. Unifying Views of Autism Spectrum
894 Disorders: A Consideration of Autoregulatory Feedback Loops. *Neuron* **89**,
895 1131-1156 (2016).

896 26. Sadakane, O. *et al.* In Vivo Two-Photon Imaging of Dendritic Spines in
897 Marmoset Neocortex. *eNeuro* **2** (2015).

898 27. Santisakultarm, T.P. *et al.* Two-photon imaging of cerebral hemodynamics and
899 neural activity in awake and anesthetized marmosets. *J Neurosci Methods* **271**,
900 55-64 (2016).

901 28. Holtmaat, A., Wilbrecht, L., Knott, G.W., Welker, E. & Svoboda, K.
902 Experience-dependent and cell-type-specific spine growth in the neocortex.
903 *Nature* **441**, 979-983 (2006).

904 29. Yasumatsu, N., Matsuzaki, M., Miyazaki, T., Noguchi, J. & Kasai, H. Principles
905 of long-term dynamics of dendritic spines. *J Neurosci* **28**, 13592-13608 (2008).

906 30. Harvey, C.D. & Svoboda, K. Locally dynamic synaptic learning rules in
907 pyramidal neuron dendrites. *Nature* **450**, 1195-1200 (2007).

908 31. Harvey, C.D., Yasuda, R., Zhong, H. & Svoboda, K. The spread of Ras activity
909 triggered by activation of a single dendritic spine. *Science* **321**, 136-140 (2008).

910 32. Murakoshi, H., Wang, H. & Yasuda, R. Local, persistent activation of Rho
911 GTPases during plasticity of single dendritic spines. *Nature* **472**, 100-104
912 (2011).

913 33. Santamaria, F., Wils, S., De Schutter, E. & Augustine, G.J. The diffusional
914 properties of dendrites depend on the density of dendritic spines. *Eur J Neurosci*
915 **34**, 561-568 (2011).

916 34. Takahashi, N. *et al.* Locally synchronized synaptic inputs. *Science* **335**, 353-356
917 (2012).

35. Noguchi, J. *et al.* Bidirectional in vivo structural dendritic spine plasticity revealed by two-photon glutamate uncaging in the mouse neocortex. *Sci Rep* **9**, 13922 (2019).

36. Ravasenga, T. *et al.* Spatial regulation of coordinated excitatory and inhibitory synaptic plasticity at dendritic synapses. *Cell Reports* **38**, 110347 (2022).

37. Belmonte, M.K. *et al.* Autism and abnormal development of brain connectivity. *J Neurosci* **24**, 9228-9231 (2004).

38. Ouyang, M., Kang, H., Detre, J.A., Roberts, T.P.L. & Huang, H. Short-range connections in the developmental connectome during typical and atypical brain maturation. *Neurosci Biobehav Rev* **83**, 109-122 (2017).

39. Falk, E.N. *et al.* Nicotinic regulation of local and long-range input balance drives top-down attentional circuit maturation. *Sci Adv* **7** (2021).

40. Holderith, N. *et al.* Release probability of hippocampal glutamatergic terminals scales with the size of the active zone. *Nat Neurosci* **15**, 988-997 (2012).

41. Penagarikano, O. *et al.* Exogenous and evoked oxytocin restores social behavior in the Cntnap2 mouse model of autism. *Sci Transl Med* **7**, 271ra278 (2015).

42. Sgritta, M. *et al.* Mechanisms Underlying Microbial-Mediated Changes in Social Behavior in Mouse Models of Autism Spectrum Disorder. *Neuron* **101**, 246-259 e246 (2019).

43. Hara, Y. *et al.* Oxytocin attenuates deficits in social interaction but not recognition memory in a prenatal valproic acid-induced mouse model of autism. *Horm Behav* **96**, 130-136 (2017).

44. Parker, K.J. *et al.* Intranasal oxytocin treatment for social deficits and biomarkers of response in children with autism. *Proc Natl Acad Sci U S A* **114**, 8119-8124 (2017).

45. Sikich, L. *et al.* Intranasal Oxytocin in Children and Adolescents with Autism Spectrum Disorder. *N Engl J Med* **385**, 1462-1473 (2021).

46. Martins, D., Paduraru, M. & Paloyelis, Y. Heterogeneity in response to repeated intranasal oxytocin in schizophrenia and autism spectrum disorders: A meta-analysis of variance. *Br J Pharmacol* **179**, 1525-1543 (2022).

47. Yamasue, H. *et al.* Effect of a novel nasal oxytocin spray with enhanced bioavailability on autism: a randomized trial. *Brain* (2022).

48. Mitre, M. *et al.* A Distributed Network for Social Cognition Enriched for Oxytocin Receptors. *J Neurosci* **36**, 2517-2535 (2016).

49. Inoue, K., Ford, C.L., Horie, K. & Young, L.J. Oxytocin receptors are widely distributed in the prairie vole (Microtus ochrogaster) brain: Relation to social behavior, genetic polymorphisms, and the dopamine system. *J Comp Neurol* **530**, 2881-2900 (2022).

50. Freeman, S.M. & Young, L.J. Comparative Perspectives on Oxytocin and Vasopressin Receptor Research in Rodents and Primates: Translational Implications. *J Neuroendocrinol* **28** (2016).

51. Parikshak, N.N. *et al.* Genome-wide changes in lncRNA, splicing, and regional gene expression patterns in autism. *Nature* **540**, 423-427 (2016).

52. Parikshak, N.N. *et al.* Integrative functional genomic analyses implicate specific molecular pathways and circuits in autism. *Cell* **155**, 1008-1021 (2013).

53. Meltzer, A. & Van de Water, J. The Role of the Immune System in Autism Spectrum Disorder. *Neuropsychopharmacology* **42**, 284-298 (2017).

54. Wilson, D.E., Whitney, D.E., Scholl, B. & Fitzpatrick, D. Orientation selectivity and the functional clustering of synaptic inputs in primary visual cortex. *Nat Neurosci* **19**, 1003-1009 (2016).

55. Bloss, E.B. *et al.* Single excitatory axons form clustered synapses onto CA1 pyramidal cell dendrites. *Nat Neurosci* **21**, 353-363 (2018).

56. McBride, T.J., Rodriguez-Contreras, A., Trinh, A., Bailey, R. & Debello, W.M. Learning drives differential clustering of axodendritic contacts in the barn owl auditory system. *J Neurosci* **28**, 6960-6973 (2008).

973 57. Hiratani, N. & Fukai, T. Redundancy in synaptic connections enables neurons to
974 learn optimally. *Proc Natl Acad Sci U S A* **115**, E6871-E6879 (2018).

975 58. Nakagami, A. *et al.* Reduced childhood social attention in autism model
976 marmosets predicts impaired social skills and inflexible behavior in adulthood.
977 *Frontiers in Psychiatry* **13** (2022).

978 59. Dominguez-Iturza, N. *et al.* The autism- and schizophrenia-associated protein
979 CYFIP1 regulates bilateral brain connectivity and behaviour. *Nat Commun* **10**,
980 3454 (2019).

981 60. Rinaldi, T., Perrodin, C. & Markram, H. Hyper-connectivity and hyper-plasticity
982 in the medial prefrontal cortex in the valproic Acid animal model of autism.
983 *Front Neural Circuits* **2**, 4 (2008).

984 61. Risher, W.C. *et al.* Astrocytes refine cortical connectivity at dendritic spines.
985 *Elife* **3** (2014).

986 62. Velmeshev, D. *et al.* Single-cell genomics identifies cell type-specific molecular
987 changes in autism. *Science* **364**, 685-689 (2019).

988 63. Velmeshev, D. *et al.* Cell-Type-Specific Analysis of Molecular Pathology in
989 Autism Identifies Common Genes and Pathways Affected Across Neocortical
990 Regions. *Mol Neurobiol* **57**, 2279-2289 (2020).

991 64. Sahin, M. & Sur, M. Genes, circuits, and precision therapies for autism and
992 related neurodevelopmental disorders. *Science* **350** (2015).

993 65. Marlin, B.J. & Froemke, R.C. Oxytocin modulation of neural circuits for social
994 behavior. *Dev Neurobiol* **77**, 169-189 (2017).

995 66. Yamasue, H. *et al.* Effect of intranasal oxytocin on the core social symptoms of
996 autism spectrum disorder: a randomized clinical trial. *Mol Psychiatry* **25**, 1849-
997 1858 (2020).

998 67. Ash, R.T. *et al.* Inhibition of Elevated Ras-MAPK Signaling Normalizes
999 Enhanced Motor Learning and Excessive Clustered Dendritic Spine
1000 Stabilization in the MECP2-Duplication Syndrome Mouse Model of Autism.
1001 *eNeuro* **8** (2021).

1002 68. Noguchi, J. *et al.* State-dependent diffusion of actin-depolymerizing
1003 factor/cofilin underlies the enlargement and shrinkage of dendritic spines. *Sci*
1004 *Rep* **6**, 32897 (2016).

1005 69. Liston, C. & Gan, W.B. Glucocorticoids are critical regulators of dendritic spine
1006 development and plasticity in vivo. *Proc Natl Acad Sci U S A* **108**, 16074-16079
1007 (2011).

1008 70. Frye, C.A. & Llaneza, D.C. Corticosteroid and neurosteroid dysregulation in an
1009 animal model of autism, BTBR mice. *Physiol Behav* **100**, 264-267 (2010).

1010 71. Lorsung, E., Karthikeyan, R. & Cao, R. Biological Timing and
1011 Neurodevelopmental Disorders: A Role for Circadian Dysfunction in Autism
1012 Spectrum Disorders. *Front Neurosci* **15**, 642745 (2021).

1013 72. Nakamura, M. *et al.* Prenatal valproic acid-induced autism marmoset model
1014 exhibits higher salivary cortisol levels. *Frontiers in Behavioral Neuroscience* **16**
1015 (2022).

1016 73. Schindelin, J. *et al.* Fiji: an open-source platform for biological-image analysis.
1017 *Nat Methods* **9**, 676-682 (2012).

1018 74. Grillo, F.W. *et al.* Increased axonal bouton dynamics in the aging mouse cortex.
1019 *Proc Natl Acad Sci U S A* **110**, E1514-1523 (2013).

1020 75. Cavanaugh, J., Huffman, M.C., Harnisch, A.M. & French, J.A. Marmosets
1021 treated with oxytocin are more socially attractive to their long-term mate. *Front*
1022 *Behav Neurosci* **9**, 251 (2015).

1023 76. Zhang, R. *et al.* Transcriptional and splicing dysregulation in the prefrontal
1024 cortex in valproic acid rat model of autism. *Reprod Toxicol* **77**, 53-61 (2018).

1025 77. Mizuno, S. *et al.* Comprehensive Profiling of Gene Expression in the Cerebral
1026 Cortex and Striatum of BTBRTF/ArtRbrc Mice Compared to C57BL/6J Mice.
1027 *Front Cell Neurosci* **14**, 595607 (2020).

1028 78. Rogers, T.D. *et al.* Effects of a social stimulus on gene expression in a mouse
1029 model of fragile X syndrome. *Mol Autism* **8**, 30 (2017).

1030 79. Zhao, D. *et al.* Transcriptome analysis of microglia in a mouse model of Rett
1031 syndrome: differential expression of genes associated with
1032 microglia/macrophage activation and cellular stress. *Mol Autism* **8**, 17 (2017).

1033 80. Phan, B.N. *et al.* A myelin-related transcriptomic profile is shared by Pitt-
1034 Hopkins syndrome models and human autism spectrum disorder. *Nat Neurosci*
1035 **23**, 375-385 (2020).

1036 81. Gordon, A. *et al.* Transcriptomic networks implicate neuronal energetic
1037 abnormalities in three mouse models harboring autism and schizophrenia-
1038 associated mutations. *Mol Psychiatry* **26**, 1520-1534 (2021).

1039 82. Tilot, A.K. *et al.* Neural transcriptome of constitutional Pten dysfunction in mice
1040 and its relevance to human idiopathic autism spectrum disorder. *Mol Psychiatry*
1041 **21**, 118-125 (2016).

1042 83. McKenzie, A.T. *et al.* Brain Cell Type Specific Gene Expression and Co-
1043 expression Network Architectures. *Sci Rep* **8**, 8868 (2018).
1044

1045